Universitá di Pisa
CdLS in Ingegneria Biomedica

Study and development of a magnetic steering system for microrobots

Master Thesis

Supervisors:

Prof. Arianna Menciassi

Prof. Paolo Dario

Virginia Pensabene, PhD

Virgilio Mattoli, PhD

Candidate:

Stefano Palagi

A.A. 2008/09

alla mia famiglia
(to my family)

Abstract

In a close future micro-scaled untethered robots might be able to access small spaces inside the human body, currently reachable only by using invasive surgical methods, thus revolutionizing future medicine. The aim of this Master Thesis work is to study and develop a system that can exploit static magnetic fields and gradients to steer purpose-developed microrobots.

A concept of the device for the generation of magnetic fields is first elaborated, moving from the state-of-art systems based on Helmholtz and Maxwell coils, which can generate, respectively, nearly uniform magnetic fields and gradients. A uniform magnetic field can be used to orient a magnetic or magnetisable object, aligning it with the direction of the field, while a uniform magnetic gradient can be used to shift such an object. The developed system is formed by two coils in the Maxwell geometrical configuration and independently powered in order to generate a uniform magnetic gradient, a quasi-uniform magnetic field or a superimposition of the two, reducing the overall complexity of the hardware with respect to the systems also employing Helmholtz coils. An analytical model of the on-axis magnetic field generated by the device and a finite element model of the field in the workspace are developed. Three microrobot prototypes are then considered: a millimetre-sized NdFeB cylindrical permanent magnet, which allows to test the maximum performances of the developed device, a polymeric microbead, which is more compatible with biomedical applications but less reactive to magnetic fields than a permanent magnet, and a polymeric nanofilm, which allows to test the steering of very anisotropic shapes, both containing iron oxide nanoparticles. Models of their interaction with magnetic fields are presented. Furthermore, a model of the motion of the three prototypes employing the developed magnetic device is presented.

The experimental set up is described, including the two coils and their support backing, the monitoring and powering circuitry and a software kit containing four graphical user interfaces for the calibration and validation of the system.

After a set of trials performed for the calibration of the magnetic-field-generating device, the system is tested in steering the microrobot prototypes. The extrapolated data are compared to the behaviours predicted by the magnetic motion models.

The abilities of the magnetic steering system and its main limits are finally examined, suggesting possible improvements of both the magnetic device and the microrobots in order to enhance their control and manipulation. In particular indications for developing the next-generation of wireless

magnetically-actuated microrobots and the relative steering systems are extrapolated.

Contents

List of Figures

List of Tables

Chapter 1

Introduction

Since the 1980's, medicine has seen a dramatic shift from the open surgery, consisting in the direct access of the surgeon hands and tools in the operative area assisted by his eye-vision, towards the use of minimally invasive procedures. Actually, minimally invasive interventions are rapidly replacing invasive surgical procedures for the most prevalent human disease conditions [30].

The three greatest killers in the developed world are heart disease, cancer, and stroke or neurovascular disease, with the last being the greatest cause of disability. After drug treatment, the primary interventional therapy for vascular diseases and an important treatment modality for cancer are endovascular image-guided interventions, which generally involve the insertion of a catheter into the femoral artery, which is then threaded under fluoroscopic guidance through the vasculature to the site of the pathology to be treated. Since minimally invasive endovascular procedures are rapidly replacing many invasive surgical procedures, it would appear to make sense that this trend would continue and be combined with advances in miniaturization. Endovascular devices will thus become finer, more patient-specific, more biocompatible, and more complex with the beginning of remotely actuated active components [30].

The initial development of remote actuation is currently happening, for example in the field of electrophysiology treatment, using remote actuating ablation catheters. To assist catheter steering and navigation, two commercial systems have been developed. Sensei^{TM}(Hansen Medical, Mountain-View,CA) is a robotic catheter control system that realizes catheter navigation by two steerable sheathes incorporating an ablation catheter. The outer and the inner sheath are both manipulated via a pull-wire mechanism by a sheath carrying robotic arm that is fixed at the patient's table. The robot arm obeys the commands of the central workstation posi-

tioned in the control room. Catheter navigation is realized using a three-dimensional joystick and allows a broad range of motion in virtually any direction. Niobe®(Stereotaxis, St.Louis, MO) realizes magnetic navigation using a special magnetic catheter. In this system, a low-intensity magnetic field (0.08 T) is applied to the patient by two permanent magnets placed on the sides of patient table. A special mapping catheter containing three inner magnets is precisely navigated inside the magnetic field by changing the orientation of the field, since the magnetic catheter must align parallel to the applied magnetic field. Both Sensei™and Niobe®systems provide for remote manipulation of the catheter, thus reducing the exposure to the radiation of fluoroscopy for the interventionalists. However, the cost of such systems could be a prohibitive factor in their utilization [31], [14]. Moreover, external magnetic fields are being proposed in the neurovascular area for guiding the accurate deployment of stents for treatment of aneurysms. The use of the existing magnetic field in MRI systems is being reported for steering catheters, too [30].

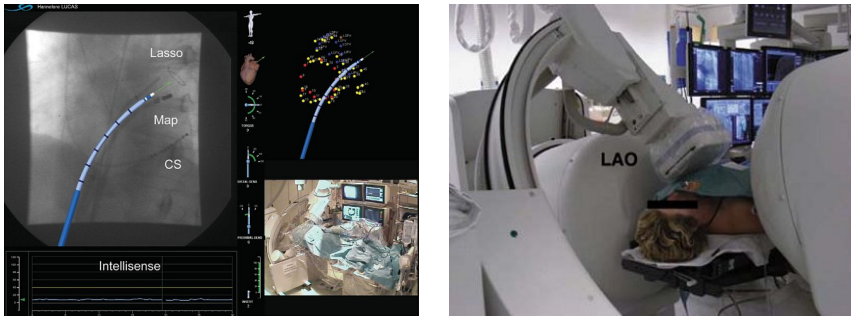

(a) *Sensei*™ (b) *Niobe*®

Figure 1.1: Catheter navigation systems

A further step in the evolution of minimally invasive endovascular applications may come from a new generation of miniaturized remote wireless controlled devices. As a matter of fact, thanks to the recent development of micro- and nano-technologies, medical procedures are evolving towards extremely targeted, localized and high precision endovascular surgery techniques performed by robotic objects even smaller than those previously described. In many cases, an untethered implementation is suitable in order to reach peculiar operative areas, such as the cardiovascular or the neural system, reducing at the same time the risks of encumbrance of blood vessels and tissue damages caused by the friction of a tethered wire, especially for complex pathways. In this framework, the design of the device starts from

the selection and fabrication of micro and nano objects able to be remotely manoeuvred and steered in small districts where they can release drugs or perform therapeutic treatments. Examples of micro-fabricated prototypes and bio-inspired microrobots are reported in the following paragraphs. Moreover the selection of proper propulsion strategy is required, in order to control the device position and motion with micrometric precision and to overcome limitations due to the environment and the forces involved at the micrometer scale. In this chapter main issues concerning passive, crawling and swimming robots are thus described.

1.1 Microrobotics and medicine

New surgical tools, capable of precise entering the human body through natural orifices or very small incisions and performing diagnostic and therapeutic procedures, are under development or at the research level. Although initially these devices would not be capable of performing tasks at a level of complexity equivalent to catheters, because of the limitations of on-board energy storage, reliability of miniaturized actuators and maximum forces which can be exerted, they could be useful for reaching remote sites, which are presently inaccessible to the existing tools. The first feasible simple tasks could include:

- diagnostic procedures;
- highly localized drug delivery;
- thermal treatment of tumours at selected sites;
- on-site delivery of magnetic resonance imaging (MRI) contrast agents;
- on-site delivery of carriers for biosensing applications;
- tissue cut off and reparation.

The procedures these devices will enable will not only result in even less trauma to the patient and faster recovery times, but will also enable new therapies that have yet been conceived [25], [21], [27].

The miniature devices are robotic systems with size ranging from micrometers up to millimetres and are thus called "microrobots". Microrobotics can be defined as the field that includes the design and fabrication of these robotic objects. But it is not simply about making traditional robots smaller. If robotics is often described as an interdisciplinary topic, microrobotics takes

this to another level: to work in microrobotics an understanding of many additional topics in physics, material science, and biology are needed [1].

The development of these novel miniature medical devices presents, in fact, a great deal of interesting and challenging topics, mainly concerning their control, propulsion and power-supply. When such microdevices are propelled, for example, in the body fluids, especially in the blood circulatory system, a very large number of remote locations in the human body become accessible. However, since the diameters of the blood vessels in the human body may vary from approximately 25 mm of the aorta down to 0.006-0.010 mm of capillaries, it is obvious that propelling wireless microrobots in such an environment with existing technologies represents a great technical challenge [21].

1.1.1 Propulsion techniques

Microrobots operate in the microscopic worldwhich is governed by the same physical laws as the macroscopic world, but in which the relative importance of the physical laws changes; this phenomena is due to the different scaling of physical effects with the typical dimensions of the objects subjected to these physical stimuli. Hence, talking about the scaling, we refer to some characteristic length L of the device of interest; we then assume that all dimensions scale linearly proportional to L. Thus, as we scale a device, its volume scales as L^3, while its surface area scales as L^2. Volume is associated with inertia, weight, heat capacity, and body forces, while surface area is associated with friction, heat transfer, and surface forces. It is the balance between volume and surface effects that leads to many of the scaling issues important in microrobotics.

Because of the scaling of physical effects, microrobots' world seems extraneous to our common way of thinking and needs non-traditional motion and propulsion strategies. Moreover, in the microscopic range, even traditional actuators and power-supply devices become unusable, caus to their size. In particular, whereas micro-fabrication technologies have accomplished the miniaturization of structural and electronic components, a corresponding breakthrough in energy storage is not been achieved. Therefore propulsion and power-supply are two of the main challenges in microrobotics and, consequently, novel technologies must be considered in the design of sub-millimetre sized robots [1].

Passive microrobots

The simplest type of microrobot is passive. This kind of robot does not contain controlled form of locomotion and simply moves as its environment dictates. A miniature medical device, for example, could be passively carried to the site of operations by means of the blood flow.

Although, designing robots at true micro scales, passive microrobots may be some of the most feasible, since they require no actuators (at least not for locomotion), and consequently have also minimal power requirements [1], their actual application in medicine is not so easy. Although its apparent simplicity, in fact, there are a number of requirements for this method of propulsion to be practical [29]:

- the users must be able to navigate the bloodstream;
- it would be difficult to remain at the site without some means of maintaining position, either by means of an anchoring technique, or by actively moving against the current;
- since a method of propulsion should allow such a device to navigate through the cardiovascular system steering independently from the direction of the blood flow, the use of the normal blood flow itself can be considered only as a complementary means of propulsion, exploitable only when the travel path is in its direction.

The above objections do not eliminate any possibility of using this technique, but they emphasize the need for at least a supplementary means of locomotion. As such, it is essential to develop active means of propulsion for microrobots [21].

Crawling microrobots

In this context, some groups proposed active mechanisms thanks to which microrobots can crawl along the surface of the blood vessels [29]. But crawling microrobots require quite complex propulsion mechanisms, and it is difficult to fabricate and power micro-scale actuators needed for crawling. One proposed solution is to grow muscle cells directly on microrobots [1].

Swimming microrobots

Thinking of a medical application in body fluids, swimming has been the focus of a great deal of microrobot research. Swimming typically refers to movement in a liquid through body deformations, but the term will be used

more loosely here to refer to any locomotion through a liquid environment [1]. Several means of propulsion embedded onto swimming microrobots was proposed and include the use of propellers, electromagnetic and jet pumps and membrane propulsion [29]. However, always thinking to medical applications, because of space constraints when operating in the cardiovascular system and the amount of torque required for propulsion against the blood flow, embedding a propulsion mechanism is not only a major task, but if feasible, it would restrict significantly the amount of volume available within such microdevices to embed MIS-based functionality [21]. Thus, researchers have proposed numerous innovative microrobotic swimming methods, many bioinspired (e.g. flagellar swimming), with the vast majority utilizing magnetic fields to wirelessly power and control the microrobot [1]. These magnetic-swimming microrobots are described in details in section 1.3.

1.2 Lessons from nature

Nature has plenty of teachings to give, especially regarding microrobots design. Microorganisms, in fact, are proofs that systems working in the microscopic domain can exhibit amazing levels of functionality [1].

Just as most microorganisms live in fluid environments, and considering the design of robots having about the same size of microorganisms and acting in a similar environment, some remarks and problems regarding the swimming of microorganisms are here presented. Moreover, bacteria that make use of magnetic fields to orientate are described. Finally, the bioinspired approach to robotic, which enables to exploit this biological knowledge in the design of microrobot, is presented.

1.2.1 Swimming at low Reynolds number

First of all, some issues relative to fluid mechanics in the micro-scales need to presented.

The Navier-Stokes equations, when combined with appropriate boundary conditions, completely define a fluid's velocity in space and time. For an incompressible fluid with constant viscosity, they are given by the vector equation

$$\rho \frac{d\vec{V}}{dt} = -\nabla p + \mu \nabla^2 \vec{V} \tag{1.1}$$

where $\vec{V}$ is the velocity vector field, p is the hydrodynamic pressure scalar field, and ρ and μ are the fluid's constant density and dynamic viscosity,

respectively. If we substitute the following non-dimensional variables

$$\tilde{x} = \frac{x}{L} \tag{1.2}$$

$$\tilde{\vec{V}} = \frac{\vec{V}}{V_s} \tag{1.3}$$

$$\tilde{t} = \frac{tV_s}{L} \tag{1.4}$$

$$\tilde{p} = \frac{pL}{\mu V_s} \tag{1.5}$$

where x is a Cartesian coordinate variable, V_s is the magnitude of the free-stream velocity, and L is a characteristic length of the object of interest, we arrive at the non-dimensional Navier-Stokes equations [1]

$$\left(\frac{\rho V_s L}{\mu}\right) \frac{d\tilde{\vec{V}}}{d\tilde{t}} = -\tilde{\nabla}\tilde{p} + \tilde{\nabla}^2\tilde{\vec{V}} \tag{1.6}$$

From this equation, we discover the Reynolds number, which is the dimensionless quantity that embodies the interaction between a fluid's inertia and viscosity as it flows around an object:

$$Re = \frac{\rho V_s L}{\mu} = \frac{V_s L}{\nu} \tag{1.7}$$

where ν is the kinematic viscosity; for water its value is $\nu \approx 1 \times 10^{-6}\,\mathrm{m^2 s^{-1}}$. The Reynolds number represents the ratio of the inertial forces to the viscous forces and when the number is small the viscous forces dominates. At low Re, we are in a world that is either very viscous, very slow, or very small. Low-Re flow around a body is referred to as creeping flow or Stokes' flow. We no longer see a transition to turbulence, even behind bluff bodies [3].

Now consider things that move through a liquid. The Reynolds number for a man swimming in water might be 104, if we put in reasonable dimensions; for a small fish it might get down to 102. For microorganisms it is about 1×10^{-4} or 1×10^{-5}. Thus, for these animals inertia is totally irrelevant. In other words, if you are at very low Reynolds number, what you are doing at the moment is entirely determined by the forces that are exerted on you at the moment, and by nothing in the past [28]. At low Re, in fact, the role of time becomes negligible; thus, the flow pattern does not change appreciably whether it is slow or fast, and the flow is reversible. Consequently, reciprocal motion (i.e., body motion that simply goes back and forth between two configurations) results in negligible net movement [3].

1.2.2 Microorganisms' swimming techniques

Microorganisms are able to swim at low Reynolds number using a variety of techniques, none of which look like macro-scale swimmers. The most

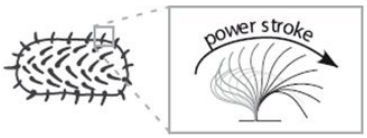

(a) *cilia*

(b) *eukaryotic flagella*

(c) *bacterial flagella*

Figure 1.2: Microorganisms' swimming techniques

widespread microorganisms' swimming techniques are based on the three following specific organelles:

- cilia: active organelles that are held perpendicular to the flow during the power stroke and parallel to the flow during the recovery stroke; many cilia are used simultaneously (Fig. 1.2a);
- eukaryotic flagella: active organelles that deform to create paddling motions, such as traveling waves or circular translating movements (Fig. 1.2b);
- bacterial (prokaryotic) flagella: they work differently than eukaryotic flagella, by using a molecular motor to turn the base of a passive flagellum 1.2c; some bacteria have multiple flagella that bundle during swimming.

All the swimming methods utilized by microorganisms capitalize on the difference in drag on a slender body normal and parallel to the slender direction as it is pulled through fluid. But all of the methods are fairly inefficient, which is not a problem because microorganisms' source of energy (food) is so plentifull [2].

1.2.3 Magneto-tactic bacteria

Many organisms have been known for a long time to sense the earth's magnetic field. Certain bacteria are also geo-magnetically sensitive. Magneto-tactic bacteria (or MTB) are a class of bacteria that exhibit the ability to orient themselves along the magnetic field lines of Earth's magnetic field. The biological phenomenon of magneto-taxis, which is an instance of magnetoception, denotes cell motility directed by a magnetic field. The term "taxis" implies that the magnetic field influences the swimming direction but not the absolute velocity of magneto-tactic cells.

These bacteria synthesize intracellular enveloped magnetic grains; these organelles are termed magnetosomes and contain magnetic crystals. Each cell behaves as though it contains a single magnetic dipole. A cell with the axis of its magnetic moment positioned at a certain angle with respect to the direction of the ambient magnetic field experiences a torque tending to align it in the field direction. Once aligned, no further magnetic forces are exerted on the cell in a uniform magnetic field like the geo-magnetic field. Thus, magneto-tactic bacteria are not pulled northward or southward by magnetic interactions; rather they are merely aligned in the external magnetic field [5].

1.2.4 Bio-inspiration

Microrobots, like microorganisms, live and swim in a low-Reynolds-number regime, thus requiring non-traditional solutions, with respect to propulsion issues, that can be inspired by nature-implemented solutions.

This bio-inspired approach to robotics consists of analyzing and understanding how biological systems work and in taking inspiration from such knowledge to design new and better robotic systems. In other words, it involves identifying the systems responsible for producing the desired characteristic, extracting the key principles underlying their biological function and translating them to a technological solution. Consequently, it is not sufficient to simply copy nature, but rather carefully choose a biological behaviour of focus, and extract the underlying principle at a level of description that is actually possible to implement.

In the next section various solutions adopted in the propulsion of microrobots in liquid environment based on wireless magnetic actuation are described. The effectiveness of bio-inspired approaches is also highlighted.

1.3 Magnetic-swimming microrobots

Although electronic and mechanical systems have been miniaturized by VLSI and MEMS technologies, no counterpart to these exists for electro-chemical energy storage. Additionally, actuators that can be used for actuation or propulsion of integrated microsystems are also lacking [37], [9]. Miniature on-board power sources are one of the most significant bottlenecks of miniature robots. Current miniature batteries continue to get smaller, more flexible, and lighter, but due to the scaling laws they deliver low power at small sizes. Micro fuel cells, MEMS-based silicon solar cells, supercapacitors, microbatteries, and radioactive thin films have been proposed as possible on-board power sources. But, still there is no feasible on-board power source for millimetre-scale or very light (less than one gram) robots [33].

Currently, the only viable option for actuating and steering a real micro-scaled robot is external energy transfer. The use of magnetic fields generated ex-vivo for energy transfer and propulsion can provide a solution to this problem. The magnetic wireless approach allows facing at the same time all the main challenging topics in microrobotics. By means of the same magnetic fields and gradients, in fact, we can control, propel and supply of power an untethered swimming microrobot.

1.3.1 Magnetic steering devices

From early times, the fascination of magnetism has inspired efforts to apply it to medicine. Magnetism alone is capable of exerting appreciable forces at quite remarkable distances, independently to intervening materials, and very likely was this that promoted people to search for ways to apply it usefully inside the human body. Furthermore, the device inside the body can be quite small and simple, and, within limits, one does not care about the complexity and power efficiency of the equipment inside the body [11].

Magnetic fields have a long history of being used to manipulate magnetic devices in the body; for examples, the extraction of ferromagnetic material from the human body by external magnets or purpose-designed electromagnets has been used since World War I (extraction of grenade splinters) [11].

In [35] we already find a first tentative to steer magnets in blood vessels.

Here some examples of device for the generation of controlled static and dynamic magnetic fields recently employed for steering microrobots or microdevices are described.

Static fields

Remote magnetic propulsion can be achieved with static magnetic fields and gradients that produce, respectively, torques and displacement forces on magnetic devices [19], [22], [37]. These magnetic fields and gradients can be generated by purpose-developed devices [37] or by MRI system [22], [21] or by Stereotaxis systems [6], to exert actions on a totally or partially magnetic, ferromagnetic or soft-magnetic miniature untethered device that moves in liquid environment.

The proposed purpose-developed devices for generating controlled magnetic fields and gradients consist of electromagnets spatial configurations. An important issue related to the control of a magnetic microrobot is the nonlinear nature of the field and gradients that are created by electromagnet coils. The field from a coil along its axis is roughly proportional to the inverse cube of the distance to the coil. Hence, the torque and force on a magnetic object, which are proportional to the magnetic field and gradient strengths respectively, scales down in even a worse way. One way of reducing the effect of such nonlinearities is to create uniform magnetic fields and field gradients using various coil configurations. For example, Helmholtz and Maxwell configurations are adopted in most state-of-art devices. The Helmholtz coil configuration consists of two identical coils that are placed on the same axis and separated by a distance equal to the radius of the coils. This arrangement generates a uniform field close to the centre of the coil pair when current passes in the same direction and with the same intensity in both coils. Similarly, the Maxwell coil configuration can generate a uniform gradient near the centre when the coils are separated by the square root of three times the radius and the current passes in the opposite direction [37]. The Helmholtz and Maxwell coils, the characteristics of fields that they generate, and their employment in a magnetic steering system are described in details in chapter 2. Both of these coils are commonly used in MRI systems, as well. Examples of devices using Helmholtz and Maxwell coils for generating controlled static magnetic fields and gradients for steering simple microrobots are shown in Fig. 1.3.

Dynamic fields

Other methods of propulsion use rotating or oscillating magnetic fields to induce motions in the object to propel through liquid environment [32], [18].

In [4] and in [38] the rotating field needed for actuating a nanocoil-shaped microrobot, inspired by bacterial flagella, is generated by superimposing sinusoidal fields to a homogeneous field, which is desirable in order to avoid

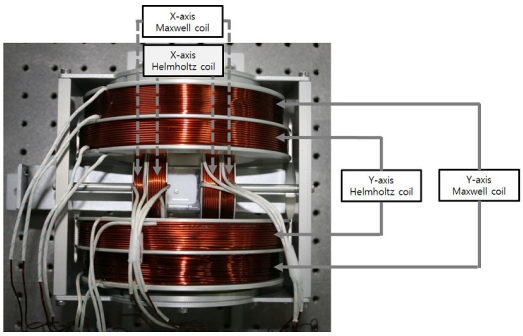

Figure 1.3: Purpose-developed devices for magnetic steering by static fields

translational magnetic forces from field gradients. For precise control of the motion of the device, the authors reported the employment of a setup that consists of three pairs of orthogonal electromagnetic Helmholtz coils. With this setup a uniform field that rotates around any direction in space is generated. Moreover, the use of Helmholtz coils allows an improvement in the homogeneity of the field, so that any translational magnetic forces are minimized. This device is shown in Fig. 1.4.

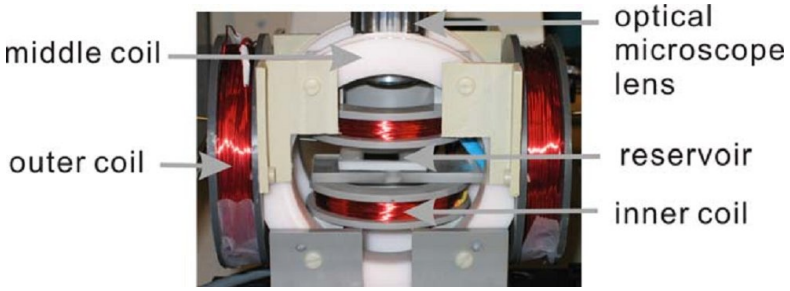

Figure 1.4: Device for generatic dynamic magnetic fields

In [34], as well, a magnetic microrobot with an elastic tail inspired to eukaryotic flagella is actuated by an alternating magnetic field generated by applying an AC voltage to an Helmholtz coil.

1.3.2 Magnetic-swimming methods

A number of robotic swimming methods have been shown to work at relatively small scales, but will have reduced effectiveness as size decreases to the microscale because they make use of reciprocating configurations. Other bio-mimetic swimming methods utilize physics that scale well to the microscale but require mechatronic components that present challenges in

micro-fabrication and wireless power and control. Several microrobots are inspired by nature and also utilize techniques that facilitate micro-fabrication and wireless power and control. Nearly every one utilizes magnetic fields. No other actuation principle offers the ability to transfer such large amounts of power wirelessly [3].

Elastic tails

Artificial eukaryotic flagella use distributed actuation to create a propagating wave. The need for distributed actuation can be somewhat overcome using a reciprocating magnetic field to generate propagating-wave-like motion in a flagellum [3]. This principle has already been proposed in [12] for actuating a magnetic catheter. Recently it has been demonstrated at the micro-scale, as well.

In [10], a flexible micro-filament, inspired by eukaryotic flagella, aligns with an external uniform magnetic field and is readily actuated by oscillating a transverse field. The homogeneous static field imposes a straight configuration to the filament, thus controlling the direction of motion; in addition, by means of the sinusoidal field with an adjustable frequency, applied in the direction perpendicular to the static field, the velocity can be controlled, as well.

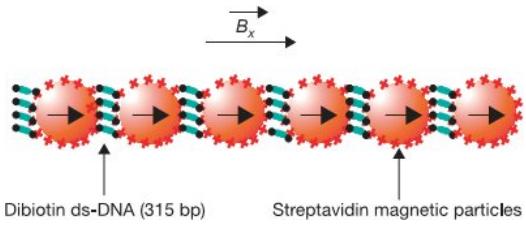

Figure 1.5: Microrobot described in [10]

The elastic tail propulsion method has also been demonstrated for few-millimetres-sized robots. In [34], a magnetic swimming mechanism (magnetic robot) is composed of a permanent ring magnet (annular neodymium magnet) and a PET filmy tail. The magnetic swimming robot is shown in Fig. 1.6. In the alternating magnetic field, the permanent magnet shows a rotational oscillation that induces a bending motion on the robot tail. During bending motions of the tail film, the robot tail presses backwards against the fluid and this pushes the robot forwards. The robot motion principle is shown in Fig. 1.6.

The same motion principle is applied also in [15] at a robot composed of a streamlined main body, made of wooden and styrol materials, containing

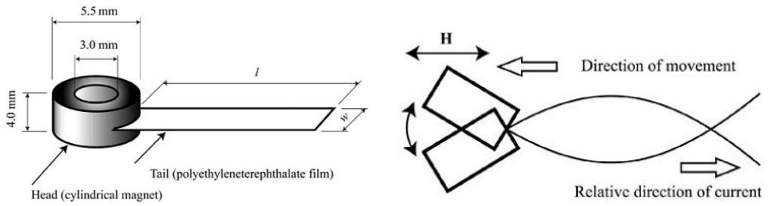

(a) *robot* (b) *working principle*

Figure 1.6: Microrobot described in [34] and working principle

a small permanent magnet and of a fin consisting of a polyimide film sheet. The robot is shown in Fig. 1.7.

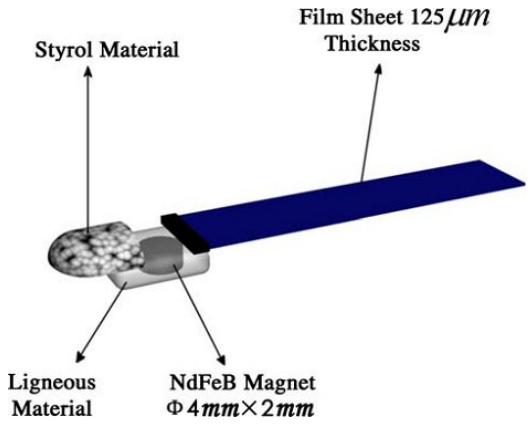

Figure 1.7: Microrobot described in [15]

Helical propellers

There is a great deal of interest in microrobot swimming using helical propellers that mimic bacterial flagella, as well. Helical propellers, in fact, can consist of a rigid structure , removing the need for the distributed actuation needed by elastic tails [3].

Swimming with helical propellers has been demonstrated for few-millimetres-sized robots. In [17] a swimming mechanism, composed of a small magnet attached to a spiral wire, is proposed. The mechanism swims propelled by waves travelling along the spiral. These waves are generated by the rotation of the magnet caused by an external alternating magnetic field, due to magnetic torque. The swimming velocity is demonstrated to increase linearly with increasing excitation frequency, and the increasing rate to depend on the shape of the spiral.

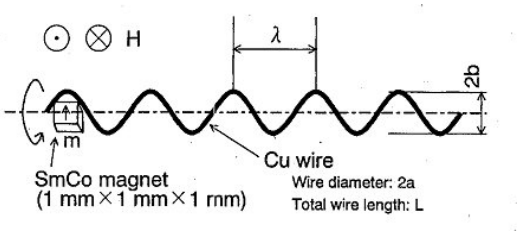

Figure 1.8: Microrobot described in [17]

Recently, the possibility to fabricate helical propellers at the microscale has been demonstrated. In [4] and in [38] a propulsion system for microrobots with similar size and motion as bacterial flagella is demonstrated. It consists of a micro-fabricated magnetic nanocoil actuated by electromagnetic fields. The magnetic torque for rotation is generated by the thin magnetic plate attempting to align with the applied field. For forward and backward motion the artificial bacterial flagella acts as a helical propeller to convert rotary motion to linear motion, thus forward and backward motion are switched by reversing the rotation direction. In contrast to reversing motion by turning the swimmer, which is the method used by bacteria and by other microscopic artificial swimmers [10], reversing the rotation direction is a more straightforward and time-efficient method.

Figure 1.9: Microrobot described in [38]

Pulling with field gradients

The last method of wireless magnetic swimming that we consider is simply pulling a rigid object through fluid using magnetic field gradients. Pulling magnetic objects with field gradients is not a bio-inspired swimming method, since a controllable external pulling source is not available to microorganisms. Furthermore, although this is a valid method to actively move through fluid, it is not technically "swimming" since it does not use the fluid to assist the propulsion [3]. However, static homogeneous magnetic fields and field gradients can be employed to apply respectively torques and forces to untethered microrobots. This greatly simplifies fabrication of microrobots since

no micro-actuator or special structure is needed for propulsion [37].

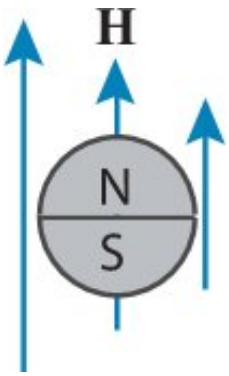

Figure 1.10: Pulling propulsion principle

This simple motion principle, schematically represented in Fig. 1.10, has been demonstrated in various works, employing both modified MRI systems [20], [21] and purpose-developed devices [37], [8], [7], to actuate small permanent magnets or soft-magnetic objects.

It is reasonable to wonder if this form of propulsion, which could not have evolved through natural selection, might outperform bio-mimetic methods. In [3], the authors compare this propulsion method with the two previously described bio-inspired methods of microrobot swimming (using magnetic fields to rotate helical propellers that mimic bacterial flagella, using magnetic fields to oscillate a magnetic head with a rigidly attached elastic tail that mimic eukaryotic flagella) considering practical hardware limitations in the generation of magnetic fields. They find that gradient pulling generally become less desirable than helical propellers and elastic tails, which have very comparable performance, as size decreases and as distance from the magnetic-field-generation source increases.

1.4 Aim of the Master Thesis work

As seen above, static homogeneous magnetic fields and field gradients are currently employed only for pulling rigid magnetic or magnetisable objects. Since pulling is considered the worst method of propulsion, if compared to bio-inspired methods that make use of dynamic magnetic fields, the reader could automatically resolve that the employment of static fields is less desirable than that of dynamic fields. But this conclusion is not so granted. While the methods of propulsion based on dynamic fields, in fact, make use of bio-inspired purpose-developed microrobots designed to exploit the

characteristics of the applied field in a full-blown "swimming" method, no bio-inspired microrobots have been designed and developed for specifically exploiting the characteristics of static magnetic fields and gradients.

Hence, the aim of this Master Thesis work is to study and develop a system that can exploit static magnetic fields and gradients to steer purpose-developed microrobots. In order to achieve this objective, first a magnetic-field-generating device similar to the state-of-art systems is designed and developed. Subsequently the actuation of a set of magnetic and magnetisable millimetre-sized objects with the developed device is tested, in order to obtain some information on which characteristics are desirable in the design of microrobot for this application.

The present work can be thus considered the preliminary stage of a more complex pathway towards the effective definition of innovative propulsion methods based on static magnetic fields and the design and development of microrobots well suited for this application. Moreover, the developed device for the generation of controlled magnetic fields is a modular platform that will be useful for future testing this new generation of microrobots.

Chapter 2

Modelling a magnetic steering system

In this Master Thesis work the wireless propulsion method based on static magnetic fields and gradients, also known as "pulling", is analysed in detail, in order to evaluate its effective limits and potentialities as part of a magnetic steering system for microrobots. Such a system, in fact, does not only consist of a device that generates magnetic fields: the microrobot that has to be propelled is an integral part of the system, too. For this consideration, studying and developing a magnetic steering system for microrobots means studying and developing a complex system composed of these two components working in full synergy.

In particular, the magnetic fields generating device and the microrobot have to be designed together, allowing that each component could exploit the main characteristics of the other.

In this chapter, the design of a device for the generation of controlled magnetic fields is described. A model of the magnetic induction field generated by the device is thus presented. Furthermore, three different objects with dimensions in the micrometers size are introduced. They are selected, designed and modified in this work in order to evaluate the possibility to use them as example of "microrobots" to be controlled with the proposed magnetic fields generating device. Their interaction with external magnetic fields is modelled and described. Finally, a model of the motion of the three prototypes employing the developed magnetic device is presented.

2.1 Model of the magnetic device

In this section the solution adopted in this work for designing a device for the generation of controlled magnetic fields is presented. The device is first conceived moving from the state-of-art systems based on Helmholtz and Maxwell coils; then a model of the generated magnetic induction field is elaborated and described.

2.1.1 Rationale

Analysing the state of art on magnetic actuation strategies, it is observed that Helmholtz and Maxwell coils are employed in the most part of the magnetic steering systems for microrobots.

The term "Helmholtz coil" refers to a device for producing a region of nearly uniform magnetic field actually composed by a coil pair [37]. A Helmholtz pair consists of two identical circular coils that are placed symmetrically one on each side of the workspace along a common axis, and separated by a distance L equal to the radius R of the coil. Each coil carries an equal electrical current flowing in the same direction.

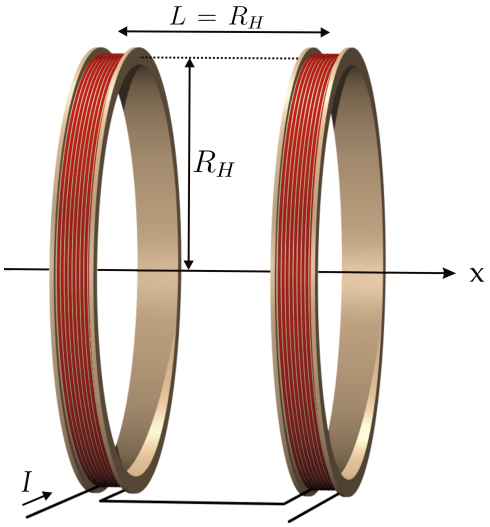

Figure 2.1: Helmholtz coil

This kind of device is employed in magnetic steering systems to generate a nearly uniform magnetic field which can be used to orient a magnetic or magnetisable object, aligning its magnetic dipole moment to the direction of the field.

The expression of the magnetic induction field along the axis of a Helmholtz coil can be obtained superimposing the field generated by the two coils. The amplitude of the on-axis magnetic induction field generated by a single wire loop of radius R and in which flows a current I can be expressed as

$$B_{single\ loop}(x) = \frac{\mu_0 I R^2}{2(R^2 + x^2)^{3/2}} \tag{2.1}$$

where x is the coordinate of the axis of the coil with origin in the centre of the loop. The field generated by a coil with N loops can be approximated multiplying the expression above by N and obtaining

$$B_{coil}(x) = \frac{\mu_0 N I R^2}{2(R^2 + x^2)^{3/2}} \tag{2.2}$$

For a Helmholtz pair we obtain

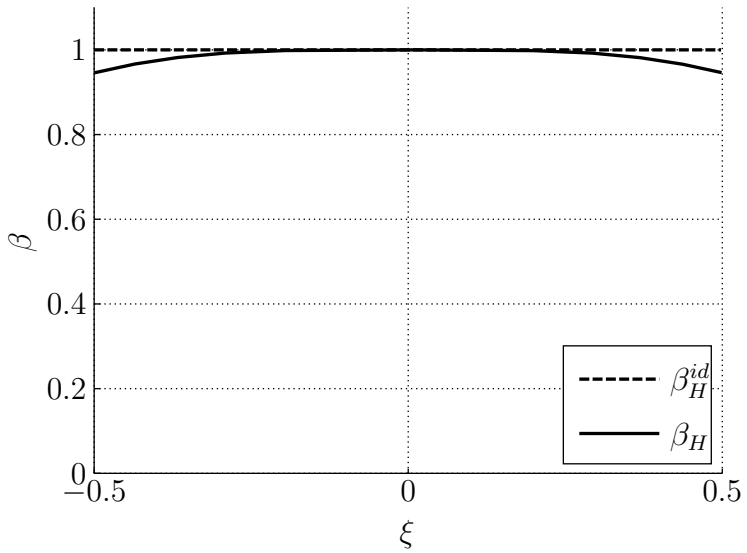

Figure 2.2: On-axis field of a Helmholtz coil

$$B_H(x) = \frac{\mu_0 N I R_H^2}{2\left[R_H^2 + (x + \frac{L}{2})^2\right]^{3/2}} + \frac{\mu_0 N I R_H^2}{2\left[R_H^2 + (x - \frac{L}{2})^2\right]^{3/2}} \tag{2.3}$$

in which x is the coordinate of the common axis of the two coils, with origin in the centre of the workspace, R_H is the radius of the coils and L the distance between them, corresponding to the length of the workspace. Considering that $L = R_H$ and using the dimensionless spatial coordinate $\xi = x/L$, the

equation 2.3 can be simplified in

$$B_H(\xi) = \frac{\mu_0 NI}{2R_H} \cdot \left\{ \frac{1}{\left[1 + \left(\xi + \frac{1}{2}\right)^2\right]^{3/2}} + \frac{1}{\left[1 + \left(\xi - \frac{1}{2}\right)^2\right]^{3/2}} \right\} \tag{2.4}$$

which, at the centre of the workspace, gives

$$B_H^0 = B_H(\xi = 0) = \frac{8}{5\sqrt{5}} \cdot \frac{\mu_0 NI}{R_H} \tag{2.5}$$

which represent the ideal constant value of the magnetic induction field generated by a Helmholtz coil. Thus, the on-axis field in the workspace of a Helmholtz coil can also be expressed in the dimensionless form as

$$\begin{aligned} \beta_H(\xi) &= \frac{B_H(\xi)}{B_H^0} \\ &= \frac{5\sqrt{5}}{16} \cdot \left\{ \frac{1}{\left[1 + \left(\xi + \frac{1}{2}\right)^2\right]^{3/2}} + \frac{1}{\left[1 + \left(\xi - \frac{1}{2}\right)^2\right]^{3/2}} \right\} \end{aligned} \tag{2.6}$$

and represented in Fig 2.2.

The term "Maxwell coil" refers, instead, to a device for producing a region of nearly uniform magnetic field gradient [37]. Similarly to the Helmholtz pair, a Maxwell pair consists of two identical circular coils that are placed symmetrically one on each side of the workspace along a common axis, but separated by a distance L equal to the square root of three times the radius R of the coil. Each coil carries an equal electrical current, here too, but flowing in opposite directions.

This device is employed in magnetic steering systems to generate a nearly uniform magnetic field gradient which can be used to pull a magnetic or magnetisable object. As in the Helmholtz coil, the expression of the magnetic induction field along the axis of a Maxwell coil can be obtained superimposing the opposite fields generated by the two coils, and can be expressed as

$$B_M(x) = -\frac{\mu_0 NIR_M^2}{2\left[R_M^2 + (x + \frac{L}{2})^2\right]^{3/2}} + \frac{\mu_0 NIR_M^2}{2\left[R_M^2 + (x - \frac{L}{2})^2\right]^{3/2}} \tag{2.7}$$

which, considering the particular length value $L = \sqrt{3}R_M$ and using the dimensionless spatial coordinate $\xi = x/L$, can be simplified in

$$B_M(\xi) = \frac{\mu_0 NI}{2R_M} \cdot \left\{ -\frac{1}{\left[1 + 3\left(\xi + \frac{1}{2}\right)^2\right]^{3/2}} + \frac{1}{\left[1 + 3\left(\xi - \frac{1}{2}\right)^2\right]^{3/2}} \right\} \tag{2.8}$$

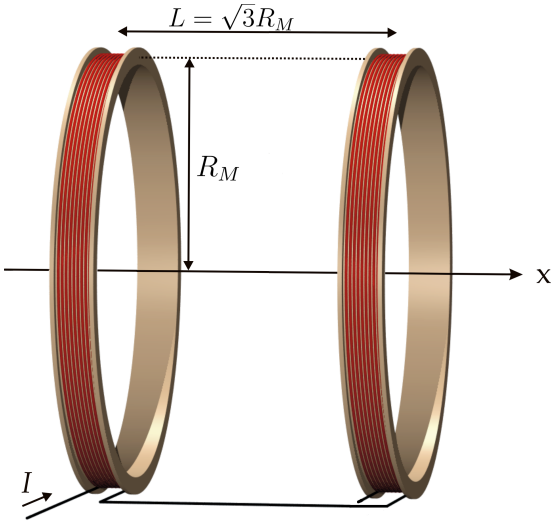

Figure 2.3: Maxwell coil

This equation can be derived to obtain the on-axis magnetic induction field gradient expressed by the following relation

(2.9)
$$\frac{dB_M(\xi)}{dx} = \frac{3\sqrt{3}}{2}\frac{\mu_0 NI}{R_M^2} \cdot \left\{ \frac{\xi + \frac{1}{2}}{\left[1 + 3\left(\xi + \frac{1}{2}\right)^2\right]^{5/2}} - \frac{\xi - \frac{1}{2}}{\left[1 + 3\left(\xi - \frac{1}{2}\right)^2\right]^{5/2}} \right\}$$

Note that, at the centre, the equations 2.8 and 2.9 give

(2.10)
$$B_M(\xi = 0) = 0$$

(2.11)
$$\nabla B_M^0 = \frac{dB_M}{dx}(\xi = 0) = \left(\frac{4}{7}\right)^{\frac{5}{2}} \frac{3\sqrt{3}}{2} \cdot \frac{\mu_0 NI}{R_M^2} = \frac{48}{49}\sqrt{\frac{3}{7}} \cdot \frac{\mu_0 NI}{R_M^2}$$

The ideal magnetic induction field generated by a Maxwell coil can thus be expressed as

(2.12)
$$B_M^{id}(\xi) = \nabla B_M^0 \cdot L\xi = \frac{144}{49\sqrt{7}}\frac{\mu_0 NI}{R_M}\xi$$

The dimensionless form of equations 2.8 and 2.12 can be calculated dividing them by the maximum ideal value of the magnetic field, expressed by

(2.13)
$$\max\left(B_M^{id}\right) = B_M^{id}\left(\xi = \frac{1}{2}\right) = \frac{72}{49\sqrt{7}}\frac{\mu_0 NI}{R_M}$$

obtaining the following equations:

$$\beta_M(\xi) = \frac{49\sqrt{7}}{144} \cdot \left\{ -\frac{1}{\left[1 + 3\left(\xi + \frac{1}{2}\right)^2\right]^{3/2}} + \frac{1}{\left[1 + 3\left(\xi - \frac{1}{2}\right)^2\right]^{3/2}} \right\} \tag{2.14}$$

$$\beta_M^{id}(\xi) = 2\xi \tag{2.15}$$

The on-axis field generated by a Maxwell coil is represented in Fig. 2.4

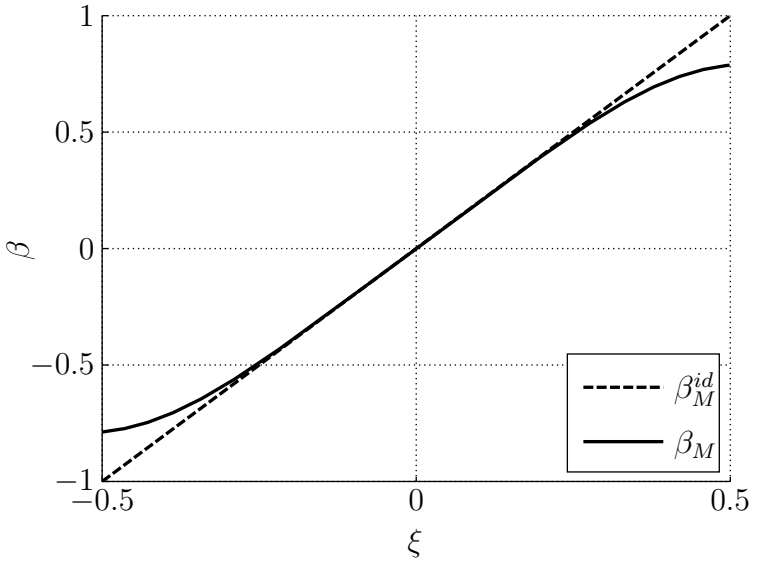

Figure 2.4: On-axis field of a Maxwell coil

In the design stage of this work, the magnetic-field-generating device can steer a microrobot in a one-dimensional workspace and it is constituted by only two identical coils arranged in the Maxwell geometrical configuration (distance between the coils equal to the square root of three times the radius of the coils). As seen above, if supplied with the same current in opposite directions, these two coils are able to generate a magnetic induction field that present a nearly uniform gradient along their common axis, like that seen in Fig. 2.4. This gradient itself could be sufficient to pull a magnetic or magnetisable object (like the microrobot prototypes seen in the previous section) backwards and forwards along one direction, but also presents the following limitations:

- the alignment to the field of a permanent magnet that we obtain, if a homogeneous aligning field is not present, is quite unstable;

- when steering a microrobot containing super-paramagnetic nanoparticles, if its centre of mass is in the exact centre of the workspace of the device, no force acts on the microrobot, because the magnetic field in its centre of mass, which is equal to the homogeneous aligning field, is null.

For these reasons all the systems in literature are constituted of at least a Helmholtz and a Maxwell coil, since that the Helmholtz coil generate a static field which allows to resolve the previously described problems.

In this work an innovative solution is adopted: moving from the consideration that two magnetic fields (like those generate by a Helmholtz and a Maxwell coil) overlap linearly and that the magnetic field generated by a coil is linearly related to the current flowing in it, it was thought to current-supply each coil independently in order to obtain the resultant field of a Helmholtz and a Maxwell coil simply superimposing the currents in the two coil which constitutes the device. In this way, the benefits of this device are that controlled overlapped fields and gradients can be generated with a single coils pair, thus simplifying the hardware.

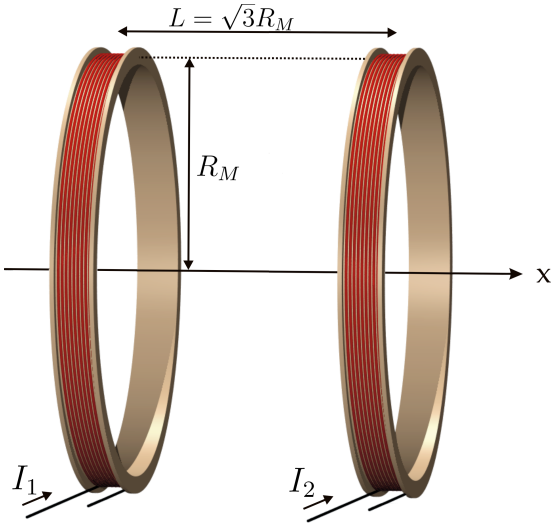

Figure 2.5: Concept of the device

The magnetic induction field along the axis of the coil generated by a Maxwell pair in which the coils are supplied with the same current (this current-supply mode is later on called "field mode") is given by

$$B_{M,fm}(x) = \frac{\mu_0 N I R_M^2}{2\left[R_M^2 + (x + \frac{L}{2})^2\right]^{3/2}} + \frac{\mu_0 N I R_M^2}{2\left[R_M^2 + (x - \frac{L}{2})^2\right]^{3/2}} \tag{2.16}$$

which, considering $L = \sqrt{3}R_M$ and $\xi = x/L$, can be simplified in the following relation

$$B_{M,fm}(\xi) = \frac{\mu_0 NI}{2R_M} \cdot \left\{ \frac{1}{\left[1 + 3\left(\xi + \frac{1}{2}\right)^2\right]^{3/2}} + \frac{1}{\left[1 + 3\left(\xi - \frac{1}{2}\right)^2\right]^{3/2}} \right\} \tag{2.17}$$

which in turn gives at the centre of the system

$$B^0_{M,fm} = B_{M,fm}(\xi = 0) = \frac{8}{7\sqrt{7}} \frac{\mu_0 NI}{R_M} \tag{2.18}$$

Note that, fixing the size L of the workspace, the current I flowing in the coils and the number of turns per coil N, the value of the magnetic induction field generated at the centre of the workspace by a Maxwell pair current-supplied in the "field mode" (eq. 2.18) is slightly higher than that generated by a standard Helmholtz coil (eq. 2.5).

A dimensionless form of the expression of the magnetic induction field can be obtained in this case, as well:

$$\begin{aligned} \beta_{M,fm}(\xi) &= \frac{B_{M,fm}(\xi)}{B^0_{M,fm}} \\ &= \frac{7\sqrt{7}}{16} \cdot \left\{ \frac{1}{\left[1 + 3\left(\xi + \frac{1}{2}\right)^2\right]^{3/2}} + \frac{1}{\left[1 + 3\left(\xi - \frac{1}{2}\right)^2\right]^{3/2}} \right\} \end{aligned} \tag{2.19}$$

With this hypothesis, even if its coils are supplied with currents with the same intensity and the same direction like in a Helmholtz coil, the field generated by a Maxwell coil cannot be considered uniform (see Fig. 2.6).

In fact, while the value of the maximum difference between the field at the centre and that at the borders of the workspace in a Helmholtz coil, obtained by the 2.4 formula, is less than 6%, in a Maxwell coil this difference exceeds 30% of the centre value, as results by the formula 2.17. This fact, which could be a limitation in an effective steering system, can be accepted in a test platform like the one developed in this work.

2.1.2 Model

Here the analytical expressions of the on-axis magnetic induction field and generated by a device constituted of two coils disposed in the Maxwell geometrical configuration and independently current-supplied, like the device developed in this work, are presented and described.

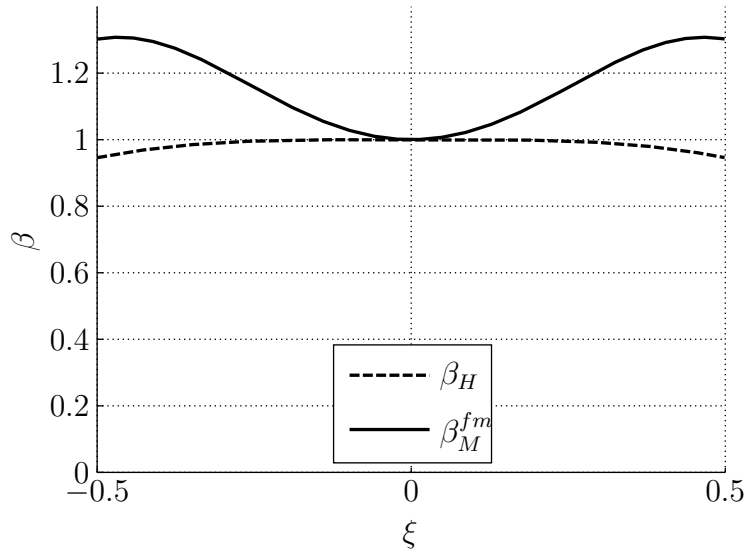

Figure 2.6: Nearly-uniform field generated by a Maxwell coil in "field mode"

The amplitude of the magnetic induction field along the common axis of the coils in function of the flowing currents can be expressed as

$$B(x, i_1, i_2) = \frac{\mu_0 N}{2R} \cdot \left\{ \frac{i_1}{\left[1 + 3\left(\frac{x}{L} + \frac{1}{2}\right)^2\right]^{3/2}} + \frac{i_2}{\left[1 + 3\left(\frac{x}{L} - \frac{1}{2}\right)^2\right]^{3/2}} \right\} \tag{2.20}$$

where i_1 and i_2 are the signed generic currents flowing, respectively, in the left (centred in $x = -L/2$) and in the right (centred in $x = +L/2$) coil. The positive verse of the currents is given by the right-hand law.

Deriving equation 2.20, we can obtain the magnetic induction field gradient along the axis of the coils in function of the currents, as expressed by

$$\frac{dB(x, i_1, i_2)}{dx} = -\frac{3\sqrt{3}\mu_0 N}{2R^2} \cdot \left\{ \frac{\left(\frac{x}{L} + \frac{1}{2}\right) i_1}{\left[1 + 3\left(\frac{x}{L} + \frac{1}{2}\right)^2\right]^{3/2}} + \frac{\left(\frac{x}{L} - \frac{1}{2}\right) i_2}{\left[1 + 3\left(\frac{x}{L} - \frac{1}{2}\right)^2\right]^{3/2}} \right\} \tag{2.21}$$

At the centre of the workspace the equation 2.20 gives

$$B_0(i_1, i_2) = \frac{\mu_0 N}{2R} \left(\frac{7}{4}\right)^{-3/2} (i_1 + i_2) = \frac{8}{7\sqrt{7}} \frac{\mu_0 N}{R} \frac{i_1 + i_2}{2} \tag{2.22}$$

while the equation 2.21 gives

$$\nabla B_0(i_1, i_2) = -\frac{3\sqrt{3}\mu_0 N}{2R^2}\left(\frac{7}{4}\right)^{-5/2}\frac{1}{2}(i_1 - i_2) = \frac{48}{49}\sqrt{\frac{3}{7}}\frac{\mu_0 N}{R^2}\frac{i_2 - i_1}{2} \tag{2.23}$$

Now, if we define the flowing currents as follows

$$\frac{i_1 + i_2}{2} = I_f \tag{2.24}$$

$$\frac{i_2 - i_1}{2} = I_g \tag{2.25}$$

which correspond to

$$i_1 = I_f - I_g \tag{2.26}$$

$$i_2 = I_f + I_g \tag{2.27}$$

we obtain, from equations 2.22 and 2.23, the following expressions

$$B_0(i_1, i_2) = B_0(I_f) = \frac{8}{7\sqrt{7}}\frac{\mu_0 N}{R} I_f \tag{2.28}$$

$$\nabla B_0(i_1, i_2) = \nabla B_0(I_g) = \frac{48}{49}\sqrt{\frac{3}{7}}\frac{\mu_0 N}{R^2} I_g \tag{2.29}$$

These two equations demonstrate that the magnetic induction field and its gradient at the centre of the workspace of a magnetic device not employing Helmholtz coils like that developed in this work are actually independent and independently controllable.

2.2 Models of microrobots

Three kinds of objects, which represent essential microrobot prototypes or possible components of micro fabricated robots, are identified. The magnetic characteristics of such objects can be modified, changing the parameters of the fabrication process, the single materials or varying the final characteristic sizes.

The three objects are a cylindrical permanent magnet with size of about one millimetre, a polymeric microbead homogenously loaded with magnetic micro particles and, finally, an ultrathin film with nanometric thickness containing magnetic particles.

The millimetre-sized permanent magnet is chosen and tested for first cause it allows to test the maximum performances of the developed device, since, fixing the volume, the magnetic dipole moment of a permanent magnet is much higher than every other fabricated device. A polymeric microbead, however, is more compatible with biomedical applications although less reactive to magnetic fields than a permanent magnet; the tests on this kind of device allows to evaluate the worsening of the steering performances with respect to the permanent magnet. Finally, with the polymeric nanofilm, the steering of very anisotropic shapes is evaluated.

In order to employ these objects as prototypes of microrobots propelled in liquid environment, their fluid-dynamic behaviour and magnetic interaction abilities are modelled and described in detail. In particular, the most important parameter to be evaluated is the drag speed that the microrobots can reach in a liquid environment, in function of the applied external magnetic field.

2.2.1 Permanent magnets

When pulling a rigid magnetic object like a permanent magnet through a Newtonian fluid, viscous fluid drag forces act on the object. The drag force F_D [37] can be expressed as

$$\vec{F}_D = -\frac{1}{2} C_D \rho_f A |\vec{v}|^2 \cdot \hat{v} \tag{2.30}$$

where ρ_f is the density of the fluid, A is the cross-sectional area of the object, $|\vec{v}|$ is the module of the relative velocity of the object with respect to the fluid, $\hat{v}$ is its versor and C_D is the drag coefficient representing the overall effect of the object's geometry on the drag force. However, the drag coefficient itself changes with the Reynolds number, Re. For a spherical or near-spherical object in laminar flow regime (low Re) the drag coefficient can be approximated as

$$C_D = \frac{24}{Re} \tag{2.31}$$

where

$$Re = \frac{\rho_f d v}{\mu_f} \tag{2.32}$$

where $d = 2r$ is the diameter of the sphere and μ_f is the dynamic viscosity of the fluid. Then, the drag force acting on a spherical or near-spherical (sphere

cross section: $A = \pi r^2$) permanent magnet pulled through Newtonian fluid at low Re can be expressed in vector form as

$$\vec{F}_D = -6\pi\mu_f r\vec{v} \tag{2.33}$$

In the present work, this equation is assumed to be also valid for a small cylindrical permanent magnet. The force generated on a whole magnetic dipole moment $\vec{m}$ (units $\mathrm{A}\cdot\mathrm{m}^2$) by an induction field B (units T) is expressed by the following equation:

$$\vec{F} = \nabla\left(\vec{m}\cdot\vec{B}\right) \tag{2.34}$$

If the object has a homogenous magnetization M ($\mathrm{A}\cdot\mathrm{m}^{-1}$) and a volume V the equation can be then rewritten as:

$$\vec{F} = V\nabla\left(\vec{M}\cdot\vec{B}\right) = V\left(\vec{M}\cdot\nabla\right)\vec{B} \tag{2.35}$$

The module $\left|\vec{M}\right|$ of the magnetization of a permanent magnet can be obtained as

$$\left|\vec{M}\right| = \frac{B_r}{\mu_0} \tag{2.36}$$

where B_r is the residual induction (or residual flux density) of the magnet and $\mu_0 = 4\pi\cdot 10^{\text{-}7}\,\mathrm{T}\cdot\mathrm{m}\cdot\mathrm{A}^{-1}$ is the permeability of free space.

The magnetic torque acting on a permanent magnet cause to an external magnetic induction field can be expressed as

$$\vec{T} = V\vec{M}\times\vec{B} \tag{2.37}$$

and is responsible to align nearly instantaneously the magnetization vector of the magnet to the direction of the applied field.

If we apply a magnetic field gradient to pull a small cylindrical permanent magnet in a Newtonian fluid at low Reynolds numbers, we obtain

$$\vec{F} + \vec{F}_D = 0 \tag{2.38}$$

and, consequently

$$\vec{F} = V\left(\vec{M}\cdot\nabla\right)\vec{B} = 6\pi\mu_f r\vec{v} \tag{2.39}$$

From this equation we can observe that, as saw in the previous chapter, at low Reynolds numbers the inertia is negligible; in fact the external force

applied to the object is linearly related to its terminal drag speed. Thus, in these conditions, the object nearly instantaneously reaches its terminal velocity where the viscous drag force exactly balances the applied magnetic force.

Finally, the terminal velocity of a cylindrical permanent magnet, with magnetization instantly aligned with the magnetic induction field, can be expressed as

$$\vec{v} = \frac{V}{6\pi\mu_f r}\left|\vec{M}\right| \cdot \nabla \left|\vec{B}\right| = \frac{rh}{6\mu_f}\left|\vec{M}\right| \cdot \nabla \left|\vec{B}\right| \tag{2.40}$$

being $V = \pi r^2 h$, with h the height of the cylinder.

2.2.2 Microbeads with super-paramagnetic particles

Polymeric spherical microbeads containing super-paramagnetic nanoparticles can be manufactured by including nanoparticle dispersion in a polymeric substrate before the polymerization stage. The embedded super-paramagnetic nanoparticles are modelled as magnetic dipoles [24] induced by an external magnetic field. In particular, their dipole moment $\vec{m}_p$ is assumed to be proportional to the local magnetic field B:

$$\vec{m}_p = \chi_p \vec{B} \tag{2.41}$$

where χ_p is a positive constant derived from the magnetic susceptibility of the nanoparticles [16]. Under this assumption, the generic particle undergoes a magnetic force that can be expressed as

$$\vec{F}_p = \nabla\left(\vec{m}_p \cdot \vec{B}\right) = 2\chi_p \vec{B} \cdot \nabla\vec{B} \tag{2.42}$$

Considering that all the embedded magnetic nanoparticles have the same size, and thus the same coefficient χ_p, the overall magnetic force can be obtained as the resultant of the forces acting on every single nano-particle embedded in the polymeric microbead:

$$\vec{F} = \sum_{i=1}^{N} \vec{F}_p^i = 2\chi_p \sum_{i=1}^{N} \vec{B}\left(x_i, y_i, z_i\right) \cdot \nabla\vec{B}\left(x_i, y_i, z_i\right) \tag{2.43}$$

where $\vec{F}_p^i$ is the magnetic force acting on the i-th particle, $\vec{B}\left(x_i, y_i, z_i\right)$ and $\nabla\vec{B}\left(x_i, y_i, z_i\right)$ are respectively the magnetic induction field and gradient in the spatial position occupied by the particle. The number of nanoparticles embedded in the polymeric bead can be defined as

$$N = d_p V \tag{2.44}$$

where d_p is the density of the particles in the bead (nanoparticles $\cdot\, \mathrm{m}^{-3}$) and V is the volume of the bead. Note that the magnetic force acting on the polymeric bead, fixing its volume, depends on the magnetic induction field gradient (like for a permanent magnet), on the magnetic characteristics and the density of the nanoparticles, which can be varied in order to obtain different sensibilities to the magnetic fields, and, especially, on the strength of the applied magnetic induction field. This aspect can be an advantage of employing micro-object with variable concentration of magnetic nanoparticles, since generally the main limitation of magnetic field generating devices (like a commercial MRI system) is the maximum gradient they can generate, rather than the strength of field. Finally, making reference again to the drag force acting on a sphere in a Newtonian fluid at low Reynolds number, expressed by equation 2.33, and summing the overall magnetic force acting on the microbead and the resistant drag force, we obtain

$$\vec{F} = 2\chi_p \sum_{i=1}^{N} \vec{B}\left(x_i, y_i, z_i\right) \cdot \nabla \vec{B}\left(x_i, y_i, z_i\right) = 6\pi\mu_f r \vec{v} \tag{2.45}$$

and, thus, the terminal drag speed of a polymeric bead containing super-paramagnetic nanoparticles can be expressed as

$$\vec{v} = \frac{\chi_p}{3\pi\mu_f r} \sum_{i=1}^{N} \vec{B}\left(x_i, y_i, z_i\right) \cdot \nabla \vec{B}\left(x_i, y_i, z_i\right) \tag{2.46}$$

2.2.3 Nanofilms with super-paramagnetic particles

Nanofilms (or nanosheets) are polymer-based films with very large area (up to tens of $\mathrm{c}^2\mathrm{m}$) and with a thickness in the order of few tens-hundreds of nanometers [13]. The possibility to include magnetic components into nanofilms, such as magnetic nanoparticles or nanobeads, represents a first step for the development of magnetic nanofilms with the potential of a remote controlled manipulation [23].

In this section we introduce a model describing the magnetic interaction between a magnetic static field and a polymeric nanofilm (homogenously filled with super-paramagnetic nanoparticles).

First of all, a fluid-dynamic model [24] of a nanofilm suspended on a fluid with density ρ_f and dynamic viscosity μ_f and moving at speed $\vec{v}$ is presented. The nanofilm can be considered as a purely two-dimensional flat plate having typical length l. At laminar regimes, the skin friction $\vec{f}_{fr}$ (force-per-length) acting on such a plate can be estimated by recalling classical fluid dynamics

results [36], namely:

$$\vec{f}_{fr} = -\frac{1}{2} C_{fr} \rho_f l \left|\vec{v}\right|^2 \hat{v} \tag{2.47}$$

where

$$C_{fr} = \frac{2\zeta}{\sqrt{Re}} \tag{2.48}$$

denotes the friction coefficient, depending on the Reynolds number $Re = \rho_f l \left|\vec{v}\right| / \mu_f$, and $\zeta = 0.664$ is a (non-dimensional) constant. We then approximate the skin friction $\vec{F}_{fr}$ on a square plate by simply multiplying $\vec{f}_{fr}$ by l, thus neglecting boundary effects. After substitution, the considered expression reads:

$$\vec{F}_{fr} = -\zeta \left(\rho_f \mu_f\right)^{1/2} \left(l \left|\vec{v}\right|\right)^{3/2} \hat{v} \tag{2.49}$$

In condition of stationary motion the drag force acting on a nanofilm pulled on a fluid is considered equal to this skin friction.

For a nanofilm containing super-paramagnetic nanoparticles dipped in a magnetic field, a magnetic force $\vec{F}_p$ due to the induced magnetic dipole moment $\vec{m}_p$ of the particle acts on each embedded particle identical to that of equation 2.42. The overall magnetic force acting on the nanofilm has the same general expression as equation 2.43, too.

Thus, for a magnetic nanofilm dragged on a fluid by means of a magnetic force we obtain

$$\vec{F} = 2\chi_p \sum_{i=1}^{N} \vec{B}\left(x_i, y_i, z_i\right) \cdot \nabla \vec{B}\left(x_i, y_i, z_i\right) = \zeta \left(\rho_f \mu_f\right)^{1/2} \left(l \left|\vec{v}\right|\right)^{3/2} \hat{v} \tag{2.50}$$

and so

$$\vec{v} = \left[\frac{2\chi_p}{\zeta \left(\rho_f \mu_f\right)^{1/2} l^{3/2}} \left| \sum_{i=1}^{N} \vec{B}\left(x_i, y_i, z_i\right) \cdot \nabla \vec{B}\left(x_i, y_i, z_i\right) \right| \right]^{2/3} \cdot \hat{F} \tag{2.51}$$

2.3 Models of the magnetic steering systems

As previously underlined, a magnetic steering system is a complex system composed of a device for the generation of controlled magnetic fields and a microrobot designed, developed and fabricated to work in full synergy. This allows obtaining the best performances from both, compensating the limits and exploiting the potentialities each other.

Here the model of the on-axis magnetic induction field generated by the developed device and the models of the magnetic motion of the three microrobot prototypes are combined, thus obtaining the models of three different magnetic steering systems.

2.3.1 The magnetic device in steering a permanent magnet

When modelling the steering system composed of the developed one-directional magnetic field generating device and of a small cylindrical permanent magnet, we can assume that the magnetization vector of the magnet is always aligned with the applied magnetic field, by means of the nearly instantaneous action of the magnetic torque expressed by equation 2.37.

The vector expression of equation 2.35 can be rewritten in the monodimensional scalar form

$$F_x = VM\frac{dB_x}{dx} \tag{2.52}$$

and, thus, the drag speed in the x direction can be expressed as

$$v_x = \frac{rh}{6\mu_f}M\frac{dB_x}{dx} \tag{2.53}$$

which, at the centre of the workspace, gives

$$v_0\left(I_g\right) = \frac{rh}{6\mu_f}M\nabla B_0\left(I_g\right) = \frac{8}{49}\sqrt{\frac{3}{7}}\frac{rhM}{\mu_f}\frac{\mu_0 N}{R^2}I_g \tag{2.54}$$

It is important to notice that the drag speed at the centre of the device depends only on the current I_g; moreover this dependence is linear. However, a current I_f have to flows in the coils in order to generate the nearly uniform magnetic field component needed for stably aligning the magnetization vector of the permanent magnet.

Considering an ideal device, which can generate really uniform magnetic fields and gradients, the drag speed can be considered constant along the workspace and equal to the value obtained at the centre. But considering the actual device, we must consider that the generated magnetic fields and gradients are not uniform, and so the obtained drag speed.

The effective drag speed along the workspace, in function of the flowing currents, can be expressed as

$$v_x\left(x, i_1, i_2\right) = -\frac{\sqrt{3}rhM}{4\mu_f}\frac{\mu_0 N}{R^2}\left\{\frac{\left(\frac{x}{L}+\frac{1}{2}\right)i_1}{\left[1+3\left(\frac{x}{L}+\frac{1}{2}\right)^2\right]^{5/2}} + \frac{\left(\frac{x}{L}-\frac{1}{2}\right)i_2}{\left[1+3\left(\frac{x}{L}-\frac{1}{2}\right)^2\right]^{5/2}}\right\} \tag{2.55}$$

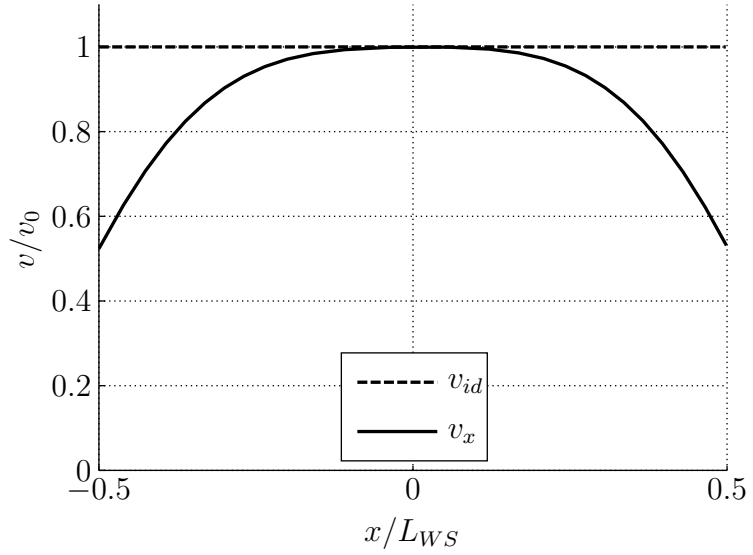

Figure 2.7: Drag speed of a permanent magnet steered by the developed magnetic device

The ideal and effective speeds of a permanent magnet steered by the magnetic device developed in the present work are shown in Fig. 2.7.

2.3.2 The magnetic device in steering a magnetic microbead

Here the one-directional steering system obtained combining the developed magnetic device and a polymeric microbead including super-paramagnetic nanoparticles is described.

Considering the magnetic field generated by the proposed device, the vector expression of equation 2.43 can be simplified as

$$F_x = 2\chi_p \sum_{i=1}^{N} B_x(x_i) \frac{dB_x(x_i)}{dx} \tag{2.56}$$

If we assume that the magnetic nanoparticles are uniformly distributed in the bead

$$dN = d_p dV = d_p A(x)\, dx \tag{2.57}$$

we obtain

$$\begin{aligned} F_x &= 2\chi_p \int_0^N B_x(x) \frac{dB_x(x)}{dx} dN \\ &= 2\chi_p d_p \int_{x-r}^{x+r} B_x(\psi) \frac{dB_x(\psi)}{d\psi} A(\psi)\, d\psi \end{aligned} \tag{2.58}$$

where

$$A(\psi) = \pi\left[r^2 - (\psi - x)^2\right] \tag{2.59}$$

denotes the cross-sectional area of the microbead at the auxiliary quote ψ and x is the coordinate of the centre of mass.

If we consider the case in which the microbead's centre of mass coincide with the centre of the workspace and we assume that, locally, a constant magnetic gradient and thus a linearly variable magnetic field are present, we obtain

(2.60)

$$\begin{aligned} F_0(I_f, I_g) &= 2\chi_p d_p \nabla B_0(I_g) \int_{-r}^{+r} \pi\left(r^2 - x^2\right)\left[B_0(I_f) + \nabla B_0(I_g)\, x\right] dx \\ &= 2\chi_p d_p V B_0(I_f)\, \nabla B_0(I_g) \end{aligned}$$

Hence, the drag speed at the centre of the workspace can be expressed as

$$v_0(I_f, I_g) = \frac{2\chi_p d_p V}{6\pi\mu_f r} B_0(I_f)\, \nabla B_0(I_g) = \frac{512\sqrt{3}}{7203} \frac{\chi_p d_p r^2}{\mu_f} \frac{\mu_0^2 N^2}{R^3} I_f I_g \tag{2.61}$$

and linearly depends on the product of the two currents I_f and I_g.

It is important to notice that, for an object containing super-paramagnetic particles, even in the ideal case in which the magnetic device produces uniform gradients, the terminal drag velocity is not constant in the workspace, but linearly variable with the x variable, as expressed by

$$\begin{aligned} v_{id}(x, I_f, I_g) &= \frac{4}{9} \frac{\chi_p d_p r^2}{\mu_f} B_{id}(x, I_f, I_g)\, \nabla B_{id}(I_g) \\ &= \frac{4}{9} \frac{\chi_p d_p r^2}{\mu_f} \left[B_0(I_f) + \nabla B_0(I_g)\, x\right] \nabla B_0(I_g) \end{aligned} \tag{2.62}$$

In the real case the expression of the terminal drag speed becomes even more complex and can be obtained by

(2.63)

$$v_x(x, i_1, i_2) = \frac{F_x(x, i_1, i_2)}{6\pi\mu_f r} = \frac{\chi_p d_p}{3\pi\mu_f r} \int_{x-r}^{x+r} B_x(\psi, i_1, i_2) \frac{dB_x(\psi, i_1, i_2)}{d\psi} A(\psi)\, d\psi$$

The effective solution is not calculated in this work. However, since the radius of the bead is quite small with respect to the second order variation of the field, we can reasonably assume that the magnetic field gradient is locally constant. With this assumption we obtain

$$v_x(x, i_1, i_2) \cong \frac{4}{9} \frac{\chi_p d_p r^2}{\mu_f} B_x(x, i_1, i_2) \frac{dB_x(x, i_1, i_2)}{dx} \tag{2.64}$$

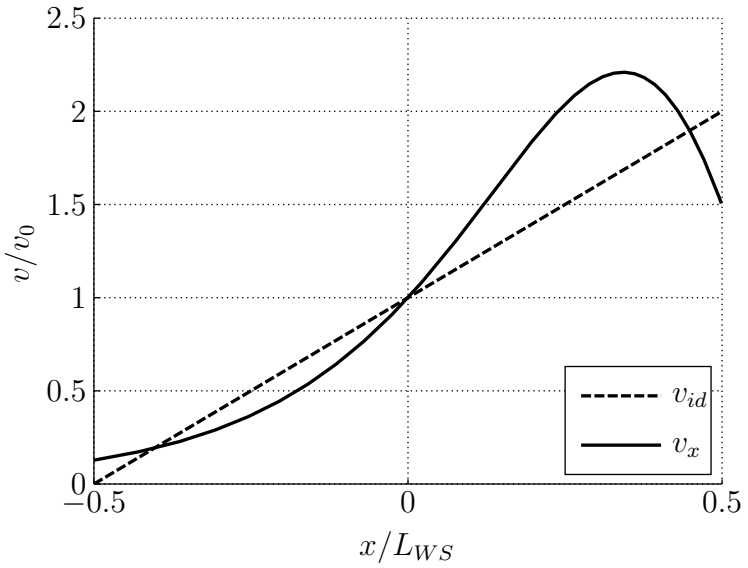

Figure 2.8: Drag speed of a microbead steered by the developed magnetic device

The constant, ideal and effective speeds of a microbead containing super-paramagnetic nanoparticles and steered by the magnetic device developed in the present work are shown in Fig. 2.8.

2.3.3 The magnetic device in steering a magnetic nanofilm

Here the one-directional steering system obtained combining the developed magnetic device and a polymeric nanofilm including super-paramagnetic nanoparticles is described.

Also in this case, considering the magnetic field generated by the proposed device, the vector expression of equation 2.43 can be simplified as in equation 2.56. If we assume that the magnetic nanoparticles are uniformly distributed in the nanofilm

$$dN = d_p dV = d_p lhdx \tag{2.65}$$

we obtain

$$F_x = 2\chi_p \int_0^N B_x(x) \frac{dB_x(x)}{dx} dN = 2\chi_p d_p lh \int_{x-l/2}^{x+l/2} B_x(\psi) \frac{dB_x(\psi)}{d\psi} d\psi \tag{2.66}$$

where x is the coordinate of the centre of mass. If we consider the case in which the nanofilm's centre of mass coincide with the centre of the workspace

and we assume that, locally, a constant magnetic gradient and thus a linearly variable magnetic field are present, we obtain

$$F_0(I_f, I_g) \cong 2\chi_p d_p hl \nabla B_0(I_g) \int_{-l/2}^{+l/2} [B_0(I_f) + \nabla B_0(I_g)\, x]\, dx \cong 2\chi_p d_p V B_0(I_f)\, \nabla B_0(I_g) \tag{2.67}$$

that is analogous to equation 2.60 seen for a microbead. It is important to notice, however, that the typical size of a nanofilm is often too large to actually neglect the effective non-linearity of the magnetic field. This formula has thus to be considered only an approximation of the real force acting on a magnetic nanofilm in the centre of the workspace. However, the approximate drag speed in this point can be calculated and assumes the following form

$$v_0(I_f, I_g) \cong \left[\frac{2\chi_p d_p V B_0(I_f)\, \nabla B_0(I_g)}{\zeta (\rho_f \mu_f)^{1/2} l^{3/2}}\right]^{2/3} = \left[\frac{768\sqrt{3}}{2401} \frac{\chi_p d_p hl^{1/2}}{\zeta (\rho_f \mu_f)^{1/2}} \frac{\mu_0^2 N^2}{R^3} I_f I_g\right]^{2/3} \tag{2.68}$$

If we assume, as usual, that the magnetic device generates an ideal constant gradient, we obtain the following expression for the ideal drag speed along the workspace

$$v_{id}(x, I_f, I_g) = \left[\frac{2\chi_p d_p hl^{1/2} B_{id}(x, I_f, I_g)\, \nabla B_{id}(I_g)}{\zeta (\rho_f \mu_f)^{1/2}}\right]^{2/3} = \left\{\frac{2\chi_p d_p hl^{1/2} [B_0(I_f) + \nabla B_0(I_g)\, x]\, \nabla B_0(I_g)}{\zeta (\rho_f \mu_f)^{1/2}}\right\}^{2/3} \tag{2.69}$$

The effective expression of the drag speed of a magnetic nanofilm steered by the developed magnetic device is not obtained in the present work. Here an approximate form, in which the non-linearity of the magnetic field into the object is neglected, is reported

$$v_x(x, i_1, i_2) \cong \left[\frac{2\chi_p d_p hl^{1/2}}{\zeta (\rho_f \mu_f)^{1/2}} B_x(x, i_1, i_2) \frac{dB_x(x, i_1, i_2)}{dx}\right]^{2/3} \tag{2.70}$$

The constant, ideal and effective speeds of a nanofilm containing superparamagnetic nanoparticles and steered by the magnetic device developed in the present work are shown in Fig. 2.9.

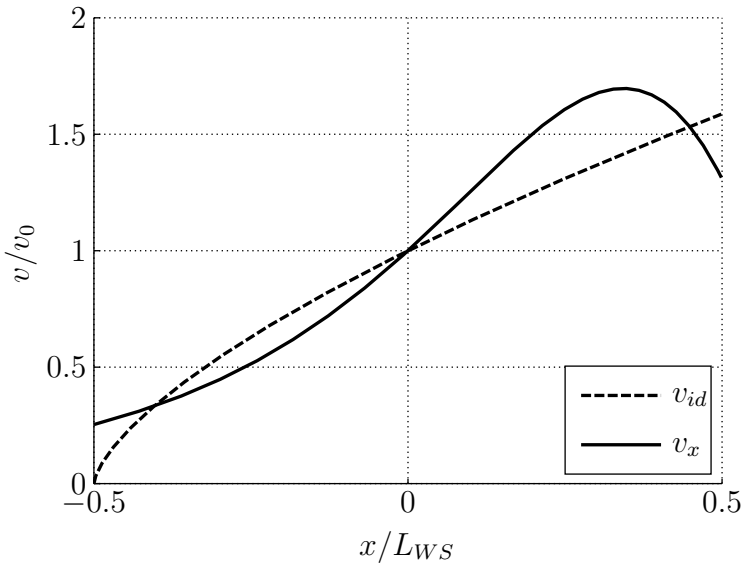

Figure 2.9: Drag speed of a nanofilm steered by the developed magnetic device

Chapter 3

Experimental set up

In this chapter the experimental set up designed for the study and development of the magnetic steering system is presented. The system is based on the pulling propulsion method.

In section 3.1, three prototypes of microrobot are described: they are conceived considering the models presented in the previous chapter and they emphasise different characteristics of the steering system.

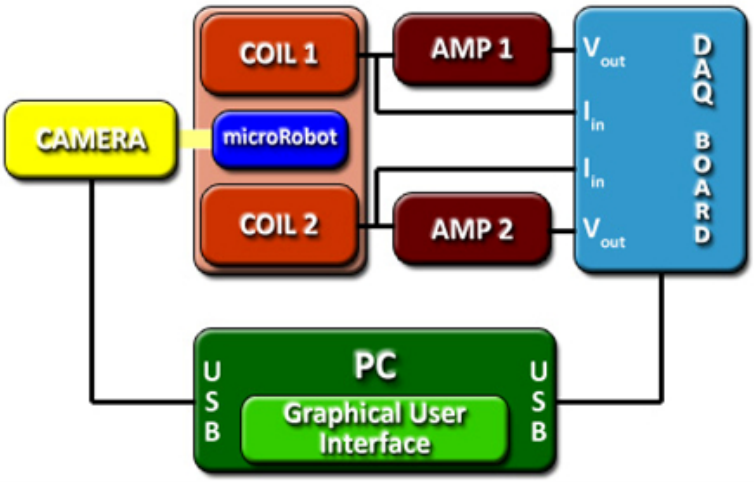

Figure 3.1: Schema of the magnetic steering system and of its components

Subsequently, the magnetic-field-generating device (see Fig. 3.1) is described in detail. The device consists of two custom electromagnets (here called coils) which surround the operative area where the microrobot can move. The input current is supplied by two purpose-designed amplification stages. These are controlled by the user through a software interface,

designed and developed for this purpose, and a USB multifunction data acquisition board. The currents that flow in the two coils are continuously monitored. The user can also monitor the microrobot steering thanks to a micro-camera placed above the workspace. The images acquired in real-time represent a visual feedback to the user.

Section 3.2 is focused on the design and fabrication of the coils while an overview on the control and monitoring hardware is given in section 3.3. Finally, the purpose developed software, which consists of the graphical user interfaces for the control and calibration of the system is described in section 3.4.

3.1 Microrobot prototypes

3.1.1 Permanent magnet

The first microrobot prototype is a cylinder neodymium permanent magnet of K&J Magnetics with 1/16" (1.5785 mm) diameter and 1/16" thickness. The volume of the cylinder is thus the following:

$$V = 3.1422\,\mathrm{mm}^3 = 3.1422 \times 10^{-9}\,\mathrm{m}^3$$

From the volume we can calculate the magnetic force acting on the magnet when dipped in a magnetic field. The magnet is in NdFeB of grade N52, with axial magnetization direction. The module of its magnetization, needed to calculate the magnetic force, too, can be directly obtained from the residual induction value (here the lower value of the range was employed, representing the worst case):

$$M = 1.1300 \times 10^6\,\mathrm{A \cdot m^{-1}}$$

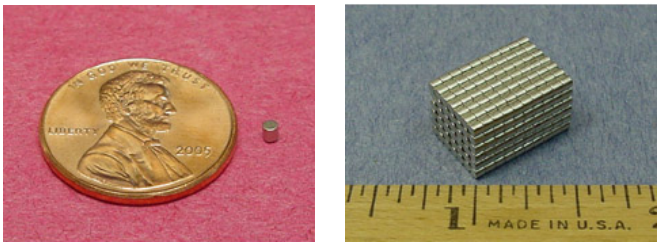

Figure 3.2: The employed cylindrical permanent magnet

3.1.2 Polymeric devices embedding magnetic particles

The other prototypes consist in a set of polymeric microbeads and in a set of nanofilms, both containing super-paramagnetic iron oxide (Fe_2O_3) nanoparticles in order to be pulled and steered by magnetic fields. The same nanoparticles with about 40 nm diameter and mass density $\rho_p = 5260\,\mathrm{kg}\cdot\mathrm{m}^{-3}$ are used both in the microbeads and in the nanofilms. A positive constant χ_p can be derived from the magnetic susceptibility, which relates the applied magnetic induction field and the magnetic dipole moment of the ferromagnetic nanoparticles.

For all the particles employed in this work the bulk susceptibility assumes the following value, obtained from SQUID measurements [24]:

$$\chi = 640\,\mathrm{A}^2\mathrm{m}^3\mathrm{N}^{-1}\mathrm{kg}^{-1}$$

This value is obtained by a rough linearization, but it can be considered accurate enough for the magnetic fields in the range of few hundreds Gauss that our device generates.

Notice that the value above is defined for a kgof nanoparticles. Knowing the size of the particles, a value for a single typical nanoparticle can be obtained, as expressed by

$$\chi_p = \chi \cdot \rho_p V_p = 1.1281 \times 10^{-16}\,\mathrm{A}^2\mathrm{m}^3\mathrm{N}^{-1}\mathrm{nanoparticle}^{-1}$$

The polymeric microbeads are little near-spherical beads of diameter of about one millimetre made of an alginate gel containing the super-magnetic particles. They are fabricated dropping an alginate solution at 1% w/v concentration, in which are suspended iron oxide particles at 1% w/v concentration, in a $CaCl_2$ solution at concentration $0.5 \times 10^3\,\mathrm{mol}\cdot\mathrm{m}^{-3}$. In presence of the bivalent positive calcium ions the alginate solution drops instantly reticulates forming gel beads embedding the ferromagnetic nanoparticles. Considering the diameter of the particles we obtain

$$d_p = \frac{C_p}{\rho_p V_p} = 5.6733 \times 10^{19}\,\mathrm{nanoparticles}\cdot\mathrm{m}^{-3}$$

Nanofilms are polymer-based films with a very large area and with a thickness of few tens-hundreds of nanometres [13]. The magnetic free-standing nanofims employed in this work are fabricated by a single step spin-coating assisted deposition (sacrificial layer approach) [26].

The magnetic nanofilms are fabricated by spin-coating assisted deposition. The preparation steps are reported here in details [23]:

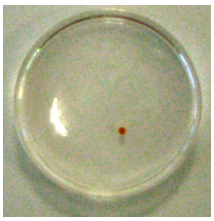

Figure 3.3: An alginate microbead containing super-paramagnetic nanoparticles

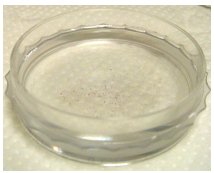

Figure 3.4: A polymeric nanofilm containing super-paramagnetic nanoparticles

1. a PVA solution ($10\,\mathrm{mg}\cdot\mathrm{ml}^{-1}$ in H_2O) is spinned at 4000 rpm for 20 s on the silicon square wafer (sacrificial layer);
2. the sample is dried on a hot plate at 80 °C for 1 min;
3. a PLLA solution ($10\,\mathrm{mg}\cdot\mathrm{ml}^{-1}$ in CH_2Cl_2) containing ferromagnetic nanoparticles is spinned at 4000 rpm for 20 s (magnetic nanofilm);
4. a nanoparticles dispersion of $10\,\mathrm{mg}\cdot\mathrm{ml}^{-1}$ is used for nanofilms procedures, from which we obtain

$$d_p = \frac{C_p}{\rho_p V_p} = 5.6733 \times 10^{19}\,\mathrm{nanoparticles}\cdot\mathrm{m}^{-3}$$

5. the sample is dried on a hot plate at 80 °C for 1 min;
6. the edges of the deposited film are defined with a cutter and the wafer putted in water: the water dissolves the sacrificial PVA layer and the magnetic nanofilm starts to float (free-standing nanofilms). Addition of PVA solution in the water acts as a stabilizer making possible nanofilm manipulation.

The obtained magnetic nanofilms are hydrophobic, free to float (free-standing) and have a surface of about $15\times15\,\mathrm{mm}^2$ and an average thickness in the order of 200 nm.

3.2 Coils

In the design stage of the device for the generation of controlled magnetic fields we have to fix the expected minimum performances of the magnetic steering systems which it belongs to and described in previous chapter.

For the magnetic-field-generating device designed in the present work we fix, for all the kinds of microrobot prototypes previously described, an arbitrary minimum drag speed of $0.2\,\mathrm{mm}\cdot\mathrm{s}^{-1}$ while suppling a typical current of 1 A.

Moving from these minimum performances the coils are dimensioned and manufactured.

3.2.1 Dimensioning

As seen in the previous chapter, using a Maxwell pair, the radius of the coils is constrained by the distance between them, which corresponds to the size of the workspace. In the design of the magnetic-field-generating device employed in this work, it is decided to have a workspace of about the same size of a small Petri dish (40 mm in diameter), in order to perform the validation tests, described in the next chapter, which consist of propulsion trials in liquid environment (in particular water). Considering the diameter of the small Petri dish, the distance between the two coils composing the Maxwell pair is fixed in the value of 45 mm and the average radius of the coils is consequently fixed in 26 mm.

Concerning the dimensioning of the coils, the minimum number of wrapping for each coil must be calculated in order to obtain the desired performances in terms of minimum value of drag speed of the microrobot prototypes. In the previous chapter, the expressions of the drag speed of all the three kinds of microrobot prototypes, in function of the applied magnetic field, are presented (2.3). Here those expressions are re-arranged in order to evaluate the minimum number of turns per coil in function of the desired minimum drag speed.

Permanent magnet

In the previous chapter we showed that the drag speed for a small cylindrical permanent magnet at the centre of the workspace in our one-dimensional magnetic steering system can be expressed (see eq. 2.54) as

$$v_0 = \frac{8}{49}\sqrt{\frac{3}{7}}\frac{rhM}{\mu_f}\frac{\mu_0 NI}{R^2} \tag{3.1}$$

where r, h and M are respectively the radius, the height and the magnetization of the permanent magnet, μ_f is the dynamic viscosity of the fluid, μ_0 is the magnetic permeability of free-space, N and R are respectively the number of turns and the radius of the coils and I is the current flowing in opposite directions in the coils (gradient-mode, $I \equiv I_g$).

Fixing the desired minimum value of the drag speed in this point, we can thus obtain an expression of the number of turns per coil in function of the parameters of the system and of the desired performances

$$N_{min} = \frac{49}{8}\sqrt{\frac{7}{3}}\frac{\mu_f R^2}{rhM\mu_0 I}v_0^{min} \tag{3.2}$$

Fixing the minimum speed and the typical value of the flowing current previously reported (respectively $0.2\,\mathrm{mm}\cdot\mathrm{s}^{-1}$ and 1 A), we get that with only a single turn per coil ($N_{min} = 1$) we can move the described small permanent magnet at a velocity higher than the desired one.

Alginate microbeads

Concerning the calculation of the minimum number of turns per coil needed for pulling the other two microrobot prototypes, it should be remind (see eq. 2.61) that the drag speed of a microdevice containing super-paramagnetic nanoparticles is proportional not only to the magnetic gradient, but also to the value of the magnetic field. For a polymeric sphere containing magnetic particles like those previously described and with the centre of mass in the centre of the workspace, we obtained the following expression of the drag speed

$$v_0 = \frac{512\sqrt{3}}{7203}\frac{\chi_p d_p r^2}{\mu_f}\frac{\mu_0^2 N^2 I_f I_g}{R^3} \tag{3.3}$$

where χ_p and d_p are respectively the susceptibility constant and the density of the particles, r is the radius of the polymeric sphere, I_f and I_g are, respectively, the absolute values of the field-mode and gradient-mode currents flowing overlapped in the coils. For more clearness it must be underlined that while in a coil flows a current $I_1 = I_f - I_g$, in the other one flows a current $I_2 = I_f + I_g$, thus creating the superimposition of a nearly-uniform magnetic field and of a nearly-uniform magnetic gradient. From this relation we can obtain the expression of the minimum number of turns per coil

$$N_{min} = \frac{49}{16}\sqrt{\frac{\sqrt{3}}{2}\frac{\mu_f}{\chi_p d_p r^2}\frac{R^3}{\mu_0^2 I_f I_g}v_0^{min}} \tag{3.4}$$

which gives, substituting the desired value of the minimum drag speed and of the typical currents, $N_{min} = 101$ turns per coil.

Nanofilms

Finally, an analogous calculation is carried out for a polymeric nanofilm containing super-paramagnetic nanoparticles, with the centre of mass in the centre of the workspace and for which we previously saw the following expression for the drag speed (see eq.2.68):

$$v_0 = \left[\frac{768\sqrt{3}}{2401} \frac{\chi_p d_p h l^{1/2}}{\zeta \left(\rho_f \mu_f\right)^{1/2}} \frac{\mu_0^2 N^2 I_f I_g}{R^3} \right]^{2/3} \tag{3.5}$$

where h and l are respectively the thickness and the typical size of the nanofilm, $\zeta = 0.664$ and ρ_f is the density of the fluid.

Fixing, as usual, the minimum drag speed and the typical values of the currents, results

$$N_{min} = \frac{49}{48} \sqrt{\frac{\sqrt{3}\zeta \left(\rho_f \mu_f\right)^{1/2}}{\chi_p d_p h l^{1/2}} \frac{\mu_0^2 I_f I_g}{R^3} \left(v_0^{min}\right)^{3/2}} \tag{3.6}$$

which gives $N_{min} = 477$ turns per coil.

Thus, as a preventive measure, it was decided for the coils to have at least five hundred turns each.

3.2.2 Manufacturing

A plastic framework is designed and manufactured as support for the two coils, which allows the positioning of the coils at the specified distance and the lodging, between them, of a Petri dish containing the microrobot prototypes used for testing the magnetic steering system. A further structure is produced for the backing of the camera above the workspace. Both the framework are visible in Fig. 3.5.

The coils of the magnetic-field-generating device are obtained spooling a 0.5 mm diameter copper wire around two dedicated backings. The spooling of the wire is hand-made while a little DC motor assists the turning of the backings; for this reason the effective parameters of the coils slightly differ from the ideal ones due to the not perfect bundling. An evaluation of the real parameters is made fitting the on-axis magnetic field measurement data and is reported in section 4.1.3. This non-idealness is considered and compensated through the main graphical user interface thanks to the independent current supply of the coils (see Appendix A).

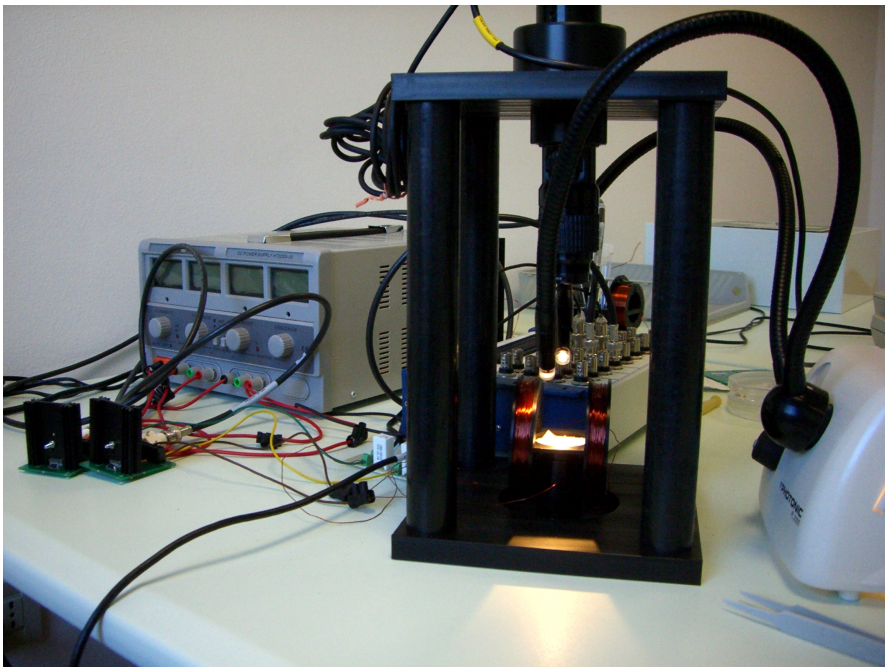

Figure 3.5: Overview of the system

3.3 Circuitry

The coils previously designed and fabricated, if adequately current-supplied, can generate the desired controlled magnetic field in the workspace. So, the control of the current supply is of extreme importance in order to control the magnetic fields and gradients requested for the propulsion of microrobots. In this section the circuitry for current-supplying and monitoring the coils is described in details. This circuitry is driven by a purpose-developed software kit (described in details in the next section) through a USB multifunction data acquisition device (National Instruments USB-6259 BNC), doted of four analogical output and sixteen analogical input channels. For all the tests carried out in this work, up to two analogical outputs and up to three analogical inputs are used.

The two outputs are employed for handling the generation of the signals for current-supplying the coils. These signals were used as inputs of two amplification circuits mounted on a Printed Circuit Board. The PCB is designed to be a multipurpose voltage amplification device and it mounts a Burr-Brown OPA549 operational amplifier.

The board has an input port (composed by $\mathsf{V_{in}}$ and GND), an output port ($\mathsf{V_{out}}$ and GND) and a power supply port ($\mathsf{V_+}$, GND and $\mathsf{V_-}$); it is supplied

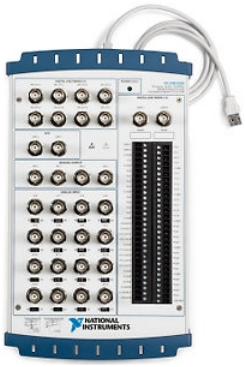

Figure 3.6: National Instruments USB-6259 BNC data acquisition board

Figure 3.7: Burr-Brown OPA549 operational amplifier

with a DC dual power supply unit. The circuit is a non-inverter amplifier with a gain chosen in the value of 4.3. The effective gain of each amplification circuit can be affected by the precision of the resistors mounted on the board; thus the effective gain factor of both the amplification circuits employed in the present work is measured as described in section 4.1.1. The fact that the amplification device is designed to be a voltage amplification board, rather than a current one, is not a limitation in this application, since, using static or nearly static fields, the current flowing in the coils can be controlled by simply controlling the applied voltage and knowing the resistance of the coils. For this reason, the effective value of the resistance of each coil is calculated from the measurement of the current flowing in the coil, as described in the next chapter. Both the gain factors and the resistances are obtained by means of dedicated GUIs included in the software kit and described in the next section. The schematic of the circuit and the drawing of the Printed Circuit Board are represented in Fig. 3.8.

In order to obtain the effective gain factors, the output of each amplification circuit is connected to an input channel of the data acquisition measuring the voltage output. For calculating the resistance of the coils, instead, two shunt resistors with nominal resistance value of $0.22\,\Omega$ are employed; the data acquisition device, in fact, can perform current measurements by connecting an input channel to the extremities of a known resistance and measuring the voltage between them. Further details on these measurements are reported

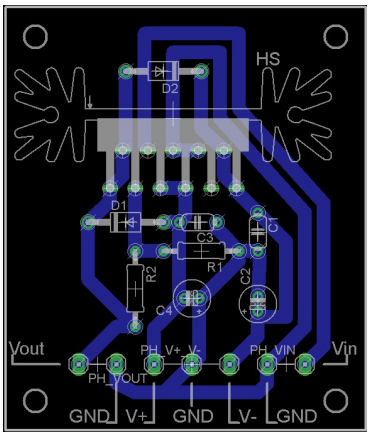

(a) *design*

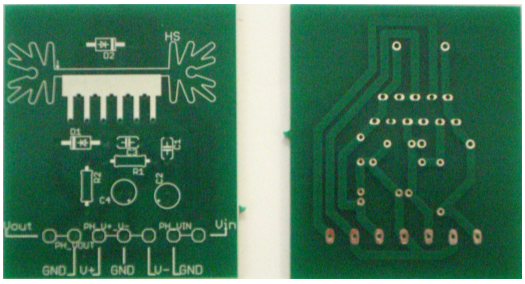

(b) *empty*

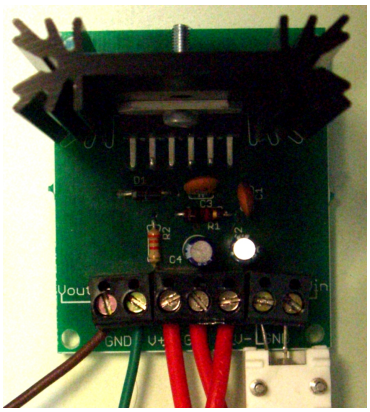

(c) *mounted*

Figure 3.8: Design of the amplification PCB

in sections 3.4 and 4.1.2.

As later on described in details, the effective magnetic induction field generated by each coil needs to be measured, in order to evaluate the real parameters of the hand-made coils. The magnetic induction field along the main axis of each coil is measured by means of a Honeywell SS94A Hall-effect sensor mounted on a dedicated support framework, power supplied with a 9 V alkaline commercial battery and connected to an analogical input channel of the data acquisition board.

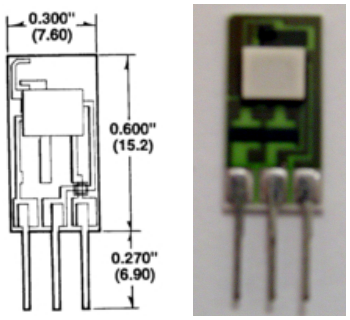

Figure 3.9: Honeywell SS94A Hall-effect magnetic field sensor

Finally, the images visualized in real-time in the trials on the microrobot prototypes are acquired with an IDS uEye USB UI-2250-MM CMOS camera able to acquire greyscale images with a maximum resolution of 1600×1200 pixels. This device is directly connected to the computer through a USB port.

3.4 Graphical User Intefaces

For allowing the control of the magnetic-field-generating device, a software kit is developed, including four Graphical User Interfaces. Three of these are service interface for system calibration and execution of the preliminary measurements (evaluation of the gain factor of the amplification circuits, evaluation of the resistance of the coils and measurement of the magnetic induction field generated by each coil along its main axis).The forth is the interface employed for driving and monitoring the magnetic steering system, as well as for data acquisition and elaboration (main interface).

3.4.1 Calibration GUIs

Three versions of the calibration interface are developed for device calibration, in order to generate actually controlled magnetic fields, and they are the following:

1. GUI for the measurement of the amplification boards' voltage output, in order to obtain the effective gain factor of each board;

2. GUI for the measurement of the currents flowing in the coil, in order to evaluate the effective values of the resistance of the coils;

3. GUI for the measurement of the on-axis magnetic field generated by each coil, for evaluating the parameters of the hand-made coils.

They are all developed by using Microsoft Visual Studio 2008 tool suite, in Visual Basic language. The data acquisition device is handled by means of the National Instruments Measurement Studio components for Visual Basic, embedded in the application. These GUIs are used for the synchronous generation of driving signals, like the voltage inputs of the amplifiers, and acquisition of the signals of interest, specific of the application of each interface.

The three interfaces are all developed from a common template and are very similar. Here this template is described in details; furthermore the solutions adopted for each particular case, which make the three interfaces substantially different, are reported.

The first two interfaces generate the same output voltage signal, as input signal for the amplifiers, on two different channels, one for each amplification board, at the same time. The same waveform is employed in the third interface, as well. This signal, characterized by a whole duration of 10 s, is a rectangular pulse of amplitude V_{in}, chosen by the code and varied in the trials, and duration of 5 s; furthermore, the signal is generated at a frequency of 1 kHz, for a total number of 10,000 samples per trial. All the generated samples are stored during generation in a dedicated "*.in" ASCII-text file.

Synchronously with the generation, a data acquisition is performed. The number of channels of acquisition and the kind of signal measured differ among the three interfaces, but for each channel 10,000 samples are acquired at 1 kHz frequency and stored in a dedicated ASCII-text file. In the interface for the evaluation of the gain factors, an acquisition of the voltage output of the amplification boards is performed on two channels, one for each board, and the acquired data are stored in two files ("*.out1" and "*.out2"). Analogously, in the interface for the evaluation of the resistance of the coils, two channels are used for the acquisition of the two flowing currents, and the data are stored in two files ("*.cur1" and "*.cur2"). For the measurement of the currents, two shunt resistances of nominal value of 0.22 Ω are employed.

The GUI developed for the measurements of the magnetic field generated by the coils is a little bit different from the other two, especially for the generated and acquired signals. First of all, the field measurement trials are

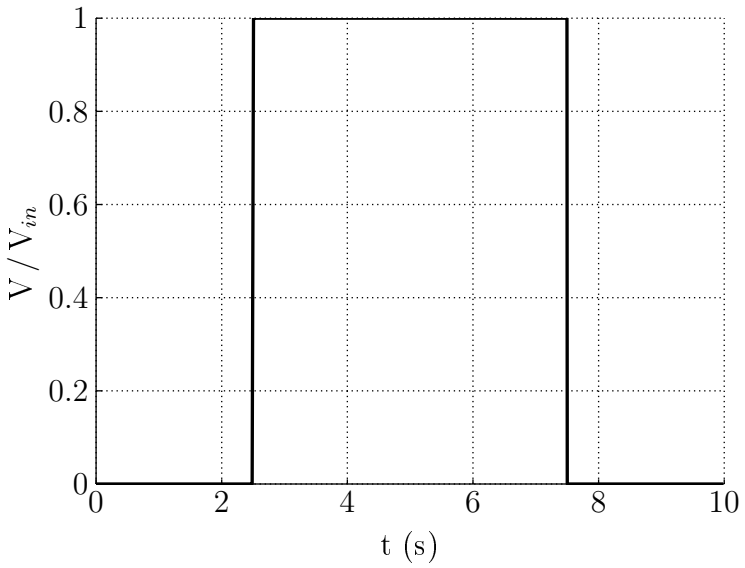

Figure 3.10: Waveform of the generated signal

performed on one coil at a time; thus only one output channel is employed. Furthermore, on the basis of the effective gain factor of the employed amplification board and of the value of the previously evaluated resistance of the tested coil, the voltage output signals are calculated in order to obtain a desired current flowing in the coil. Thus, the generated output signal differs between the coils, while, for each coil it does not change during the trials. The acquired data consist in the effective flowing current and in the magnetic induction field measured at various positions along the axis of the tested coil. The measurement of the current could actually have not to be performed, but this redundant information is retained to be important not only for fine evaluating the real parameters of the coils, but also for verifying the reliability of the previously estimated parameters (gain factors and resistances).

In all the three interfaces, the generated and acquired data are visualized, respectively, in real-time on two graphs. Furthermore, the folder and a common name for the files saved during a single trial can be chosen. Finally, every interface has an on/off switch and a led for signalling the activity of generation/acquisition process.

Further details on the employment of these graphical user interfaces in the trials and on the analysis of the acquired data are reported in the chapter 4.

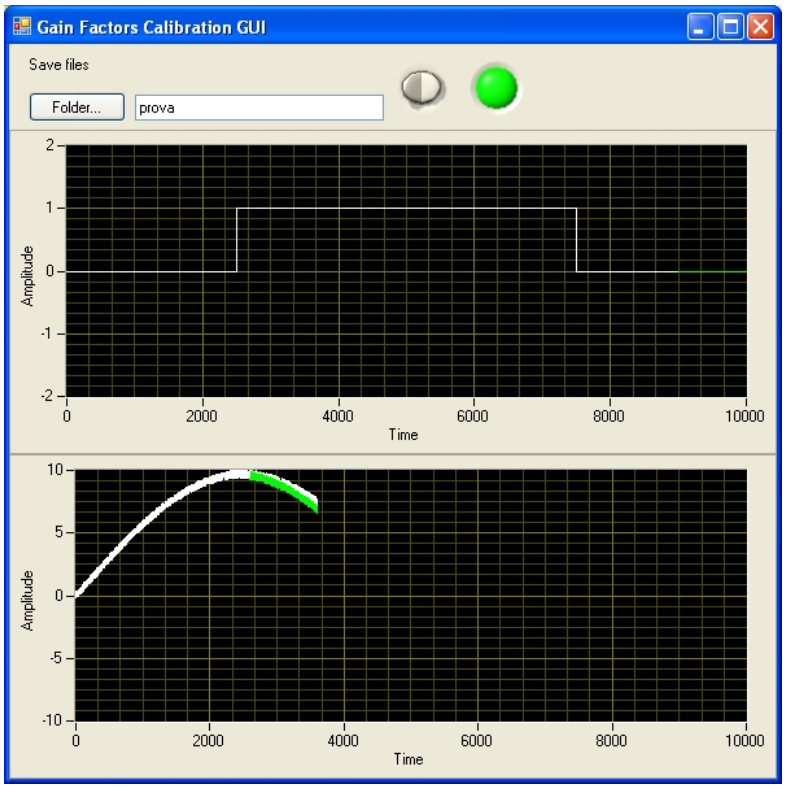

Figure 3.11: One of the three calibration GUIs

3.4.2 The main GUI

The main graphical user interface is a software tool quite more complex than the previously described calibration interfaces, since it is not only a signal generation, acquisition and visualization tool, but also a platform for the calculation of the needed input signals of the amplifiers, moving from the desired drag speed of a specified microrobot prototype, and for the elaboration, visualization and storage of the data extracted from the images acquired in real-time. The interface, as those described in the previous subsection, is developed by using Visual Basic language. Furthermore, various external components are employed for carrying it out.

The interface is constituted by two tabs (or pages). The first tab is dedicated to the execution of the trial. Since the loading of the main program window, the images acquired in real-time by the camera above the workspace are displayed by means of a uEyeCam ActiveX control embedded in the right bottom corner of the page. Selecting the type of microrobot prototype and specifying its sizes and the desired drag speed at the centre of the workspace

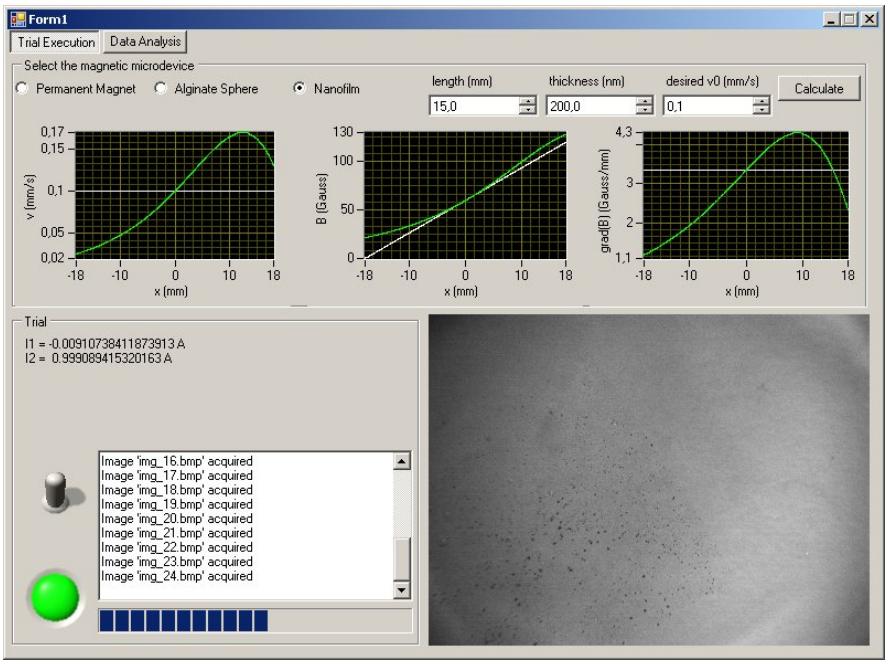

Figure 3.12: Execution of the trial

from the selection group box in the top of the tab, the program calculates and visualizes the currents that have to flow in the coils for generating the requested magnetic field. The ideal and expected drag speed, magnetic induction field and gradient are calculated along the workspace and visualized in three different graphs. These calculations, reported in details in Appendix A, are performed before the effective execution of the trial by calling an external script, previously written in Mathworks Matlab 7.1(R14), by means of a Matlab object created by the code during the loading of the main window of the program, and they enable the execution of the specified trial. This can be actually launched through an on/off switch, and its effective running is signalized with a lighted green led. During the execution of the trial the following operations are automatically performed:

- continuous generation of the currents calculated in the preliminary stage, by means of a dedicated National Instruments Measurement Studio control embedded in the program;
- acquisition and saving of the images of the workspace at a frequency of 10 fps through the uEyeCam ActiveX control;
- acquisition, monitoring and storage of the effective currents flowing in the coils, synchronously with the acquisition of the images, by means of

another dedicated National Instruments Measurement Studio control;

- continuous feedback to the user on the progress of the trial.

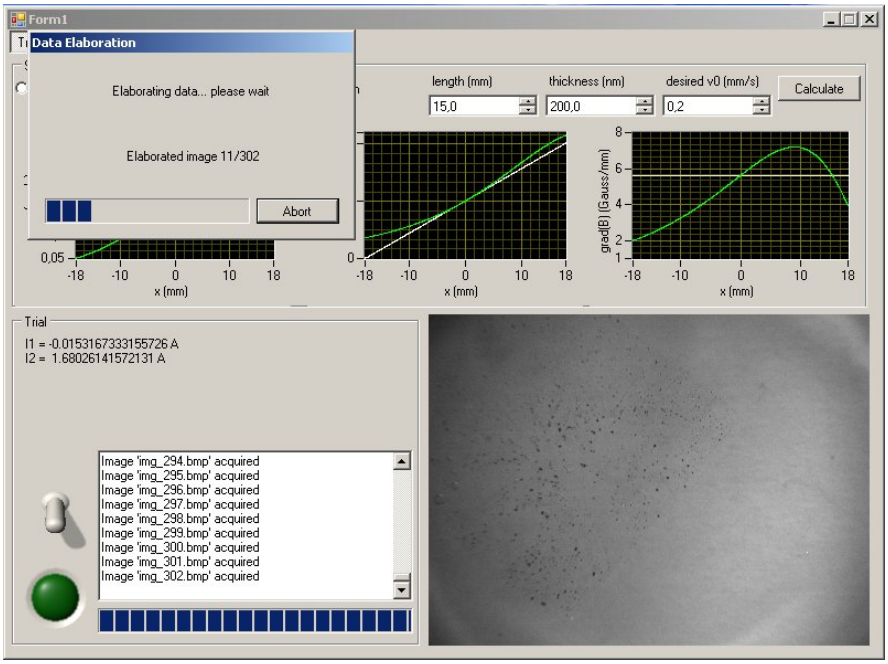

Figure 3.13: Dialog window

The trials have a fixed duration, after which all the operations described above are stopped and the data elaboration starts. During this stage the acquired images are analysed by another external purpose-developed Matlab script, in order to extract the position of the tested magnetic microdevice in every image. This data are subsequently elaborated and the effective drag speed during the execution of the trial is extracted. The measurements of the effective flowing currents are performed, as well, in order to evaluate the effective magnetic induction field and its gradient. All these calculations are reported in details in Appendix B. During all these operations the progress of the elaboration process is visualized through a dialog window. So, the obtained data are displayed in the graphs on the second page of the interface, fully dedicated to the visualization of the results, and stored in a data file for further elaborations.

Figure 3.14: Data visualization

Chapter 4

Trials and experimental results

This chapter reports all the tests and the trials carried out in the present work. Section 4.1 is dedicated to the tests performed on the developed magnetic fields generator in order to find the right tuning parameters. Three models of magnetic steering systems are presented in chapter 2; the trials performed for validating these models are thus described in section 4.2.

4.1 Tuning of the magnetic device

Many factors can influence the reliability and the accuracy of a device for the generation of magnetic fields like the one designed and developed in this work. If not properly considered and accurately compensated, non-idealness can make inconsistent outcome and invalidate the obtained results.

In order to individuate and compensate such kind of problem and to tuning the magnetic-field-generating device, a set of dedicated tests are performed.

4.1.1 Calibration of the amplification boards

The device developed in this work makes use of two custom driver boards to current-supply the coils through the amplification of a signal generated by means of a USB multifunction data acquisition device (National Instruments USB-6259) and a dedicated interface. Thus, the voltage applied to each coil, which determines the current flowing, needs to be accurately known. This voltage is given by the output signal generated by the data acquisition board multiplied the gain factor of the considered driver circuit, which depends on the actual value of the resistors mounted on the board. Consequently, the effective value of the gain factor, which can vary quite considerably from the

ideal one, needs to be properly evaluated.

Thus, the first test has been done to obtain the effective value of the gain factors of the two designed and developed boards.

For the execution of this test the dedicated user interface described in the previous chapter is used. Through it, two identical signals, used as voltage inputs of the two amplifiers, are synchronously generated and the voltage output signals of both the amplification boards are acquired, visualized and saved in dedicated files. The stored data are then analysed and elaborated in Mathworks Matlab to obtain the effective values of the gain factors.

The input signal of the amplifiers is a ten seconds waveform with a centred rectangular pulse of duration of five seconds and amplitude V_{in}, for a whole number of ten thousand samples for each trial. The amplitude V_{in} is made varying in the trials from $-2\,\mathrm{V}$ to $+2\,\mathrm{V}$ with intervals of $0.4\,\mathrm{V}$, thus performing eleven trials. For each trial ten thousand samples of the output voltage of both the amplification boards are acquired synchronously with the generation of the input signal. An independent null measure is performed before the described trials, in order to evaluate an eventual offset due to the measurement process. The evaluated offsets for the two acquisition channels are actually negligible with respect to the measured signals.

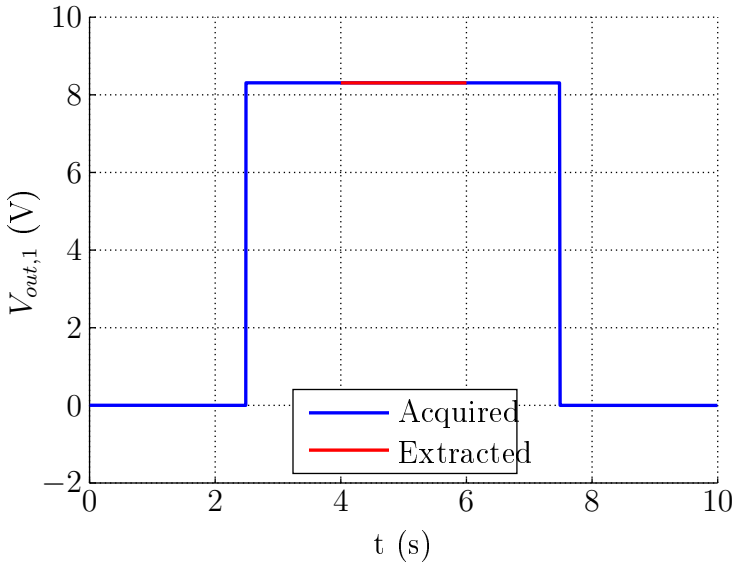

Figure 4.1: Calibration of the amplification boards: example of acquired and extracted samples

The data stored in the three dedicated files are then imported and analysed in Matlab. For each ten thousand samples, two thousand samples in the centre of the rectangular pulse are extracted; in this way distortion effects

eventually present in the step transition are discarded. Even if negligible, the null offsets previously evaluated are then subtracted from the sets of two thousands samples acquired for each value of V_{in}. The mean value and the standard deviation of each set of samples are then calculated. These values are reported in Table 4.1.

V_{in}(V)	$V_{out,1}$(V)	σ_1(mV)	$V_{out,2}$(V)	σ_2(mV)
−2.0	−8.3082	0.5658	−8.5799	0.5930
−1.6	−6.6464	0.5626	−6.8640	0.6076
−1.2	−4.9853	0.5697	−5.1491	0.5951
−0.8	−3.3230	0.5388	−3.4326	0.5814
−0.4	−1.6616	0.5428	−1.7169	0.6008
0.0	−0.0001	0.5814	−0.0000	0.5374
+0.4	+1.6616	0.5579	+1.7144	0.6161
+0.8	+3.3222	0.5863	+3.4305	0.6160
+1.2	+4.9843	0.5913	+5.1453	0.6210
+1.6	+6.6452	0.5789	+6.8603	0.6044
+2.0	+8.3075	0.5895	+8.5768	0.6115

Table 4.1: Calibration of the amplification boards: experimental data

So, excluding the standard deviation values, we obtain three sets of eleven values, one of the input signal of both the amplifier and two of their output signals. These are fitted to a linear equation of the kind

$$y = A \cdot x$$

obtaining the following two equations

$$\begin{aligned} V_{out,1} &= A_1 \cdot V_{in} \\ V_{out,2} &= A_2 \cdot V_{in} \end{aligned}$$

where the parameters A_1 and A_2, returned by the fitting routine, represent the gain factors of the two amplification boards and assumes the values

$$A_1 = 4.1538$$

$$A_2 = 4.2891$$

The experimental data, as well as the returned fitting curves for both the amplification boards are represented in the following figure.

The goodness of fit is evaluated and returned by the routine, as well. For the first amplifier we obtain an R^2 value of 1.0000 with 10 degrees of

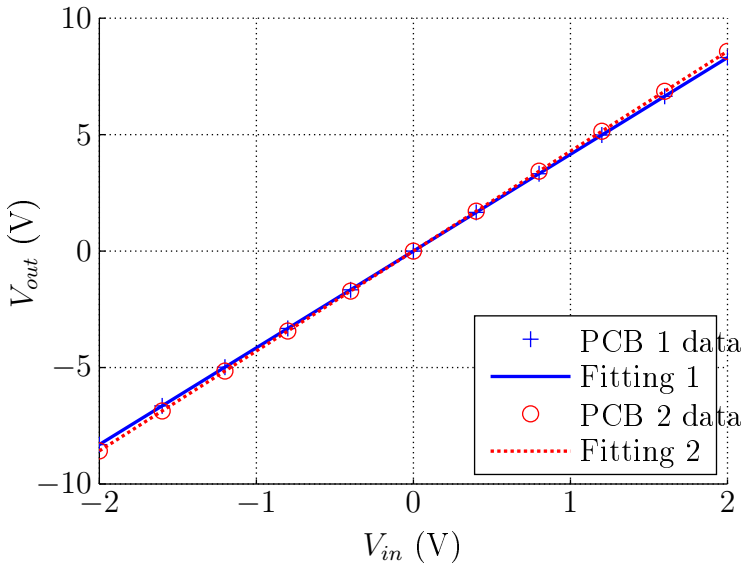

Figure 4.2: Calibration of the amplification boards: fitting

freedom. For the second amplification board the R^2 coefficient and the degree of freedom assumes the same value. The fit is very good, demonstrating the extreme linearity of the relation between the input and the output voltage of the amplification boards. This test demonstrates that the two gain factors slightly differ each other and from the theoretical ideal value of 4.3. In particular, the gain factor of the first amplification board differs for the ideal value of more than 3%.

4.1.2 Evaluation of the resistance of the coils

Since the magnetic device employs voltage amplification boards, in order to accurately generate controlled magnetic fields, and thus currents, the values of the resistances of the coils needs to be known. For this reason a test for the evaluation of such values is performed and here described.

This test is analogous to the previous one. By means of a dedicated interface, two identical voltage signals are generated at a time and used as inputs for the amplifiers. A coil in series to a shunt resistance of nominal value of $0.22\,\Omega$ (the effective values of all the employed shunt resistance are measured for the trials) is connected to the output of each amplification board. Synchronously, with the generation of the voltage signals, the values of the currents flowing in the coils are acquired by measuring the voltage on the two shunt resistances. The acquired data are then displayed in the interface and stored in dedicated files for the subsequent elaboration.

The input signal of the amplifiers is analogous to the one used in the previous test: ten thousand samples for each trial are thus generated. As before, the amplitude V_{in} is made varying in the trials from 0 V to +3.5 V with intervals of 0.5 V, for a whole number of eight trials. For each trial ten thousand samples of the currents flowing in the coils are acquired, as well. An independent null measure is performed in order to evaluate an eventual offset due to the measurement process. The evaluated offsets for the two acquisition channels are also in this case negligible with respect to the measured signals.

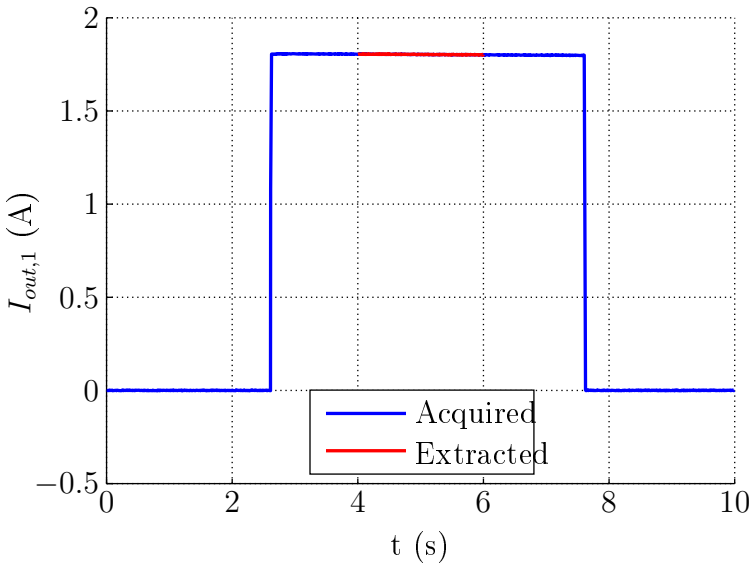

Figure 4.3: Evaluation of the resistance of the coils: example of acquired and extracted samples

The data stored in the three dedicated files are then imported and analysed in Matlab analogously to the previous test. Hence, for each ten thousand samples, two thousand samples in the centre of the rectangular pulse are extracted, in order to discard distortion effects eventually present in the step transition. The null offsets previously evaluated are then subtracted from the sets of two thousands samples acquired for each value of V_{in}. The mean value and the standard deviation of each set of samples are then calculated and reported in Table 4.2. From the voltage input of the amplifier, knowing the gain factors previously evaluated, the voltage applied to the coils are also calculated.

So, excluding the standard deviation values, we obtain four sets of eight values, two of the output signal of both amplifiers and two of the currents in

V_{in}(V)	$V_{out,1}$(V)	$V_{out,2}$(V)	I_1(A)	σ_{I_1}(A)	I_2(A)	σ_{I_2}(A)
0.0	0.0000	0.0000	0.0000	0.0006	0.0000	0.0006
0.5	2.0769	2.1445	0.2293	0.0006	0.2385	0.0006
1.0	4.1538	4.2891	0.4590	0.0006	0.4767	0.0006
1.5	6.2307	6.4337	0.6882	0.0006	0.7143	0.0006
2.0	8.3076	8.5782	0.9164	0.0007	0.9512	0.0006
2.5	10.3845	10.7228	1.1435	0.0007	1.1867	0.0007
3.0	12.4614	12.8673	1.3686	0.0009	1.4200	0.0010
3.5	14.5383	15.0118	1.5887	0.0013	1.6479	0.0013

Table 4.2: Evaluation of the resistance of the coils: experimental data

the two coils. Fitting the current data to a linear equation of the kind

$$y = \frac{1}{R} \cdot x$$

we obtain the following two equations

$$\begin{aligned} I_1 &= \tfrac{1}{R_1^*} \cdot V_{out,1} \\ I_2 &= \tfrac{1}{R_2^*} \cdot V_{out,2} \end{aligned}$$

where the parameters R_1^* and R_2^*, returned by the fitting routine, respectively represent the series of a shunt resistance (actual value) and of the resistance of a coil, as expressed by

$$\begin{aligned} R_1^* &= R_1 + R_{S1} \\ R_2^* &= R_2 + R_{S2} \end{aligned}$$

from which we obtain

$$R_1 = 8.8719\,\Omega$$

$$R_2 = 8.8288\,\Omega$$

The experimental data, as well as the returned fitting curves for both the amplification boards are represented in Fig. 4.4.

The goodness of fit is evaluated and returned by the routine, as well. For both the coils we obtain a value for the R^2 coefficient of 0.9999 with 7 degrees of freedom.

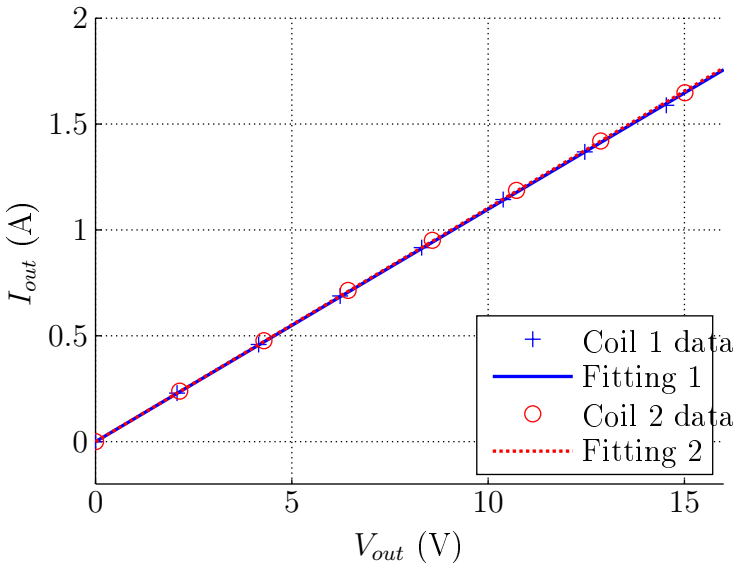

Figure 4.4: Evaluation of the resistance of the coils: fitting

4.1.3 Calibration of the magnetic field

By means of the two tests described above, we accurately know the value of the currents flowing in the coils of the magnetic device in function of the voltage used as input signal for the amplifiers. However, we need to generate accurately controlled magnetic fields and, thus, we need to evaluate the parameters of the fabricated coils.

At this purpose, the magnetic field generated by each coil along its main axis when a constant current flows is measured by means of the previously described Hall-effect magnetic field sensor. The values of the field are acquired at positions varying from 0 to 40 mm of distance from the centre of each coil, along the axis, with steps of 2 mm, for a total of 21 measures per coil. In all the trials the current flowing in the coils is fixed to 1 A, from which the needed values of Vin for each coil are calculated moving from the parameters previously obtained (gain factors of the amplification boards and resistances of the coils). The signal generation strategy is analogous to that adopted in the previous tests: a 10 s signal with a centred pulse of duration 5 s and magnitude V_{in} is generated for each trial. The values of the magnetic field and of the effective current flowing in the tested coil are acquired synchronously. One coil at a time is tested. All the acquired data are stored in dedicated files for the subsequent elaboration.

In the data elaboration stage the values of the current and of the magnetic field at each position are obtained as average values of the two thousand central samples of the ten thousand acquired for each measure. The zero-

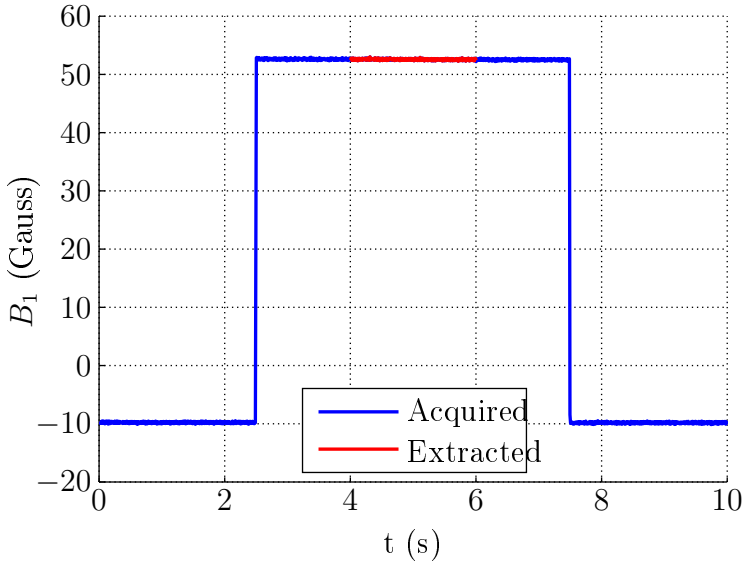

Figure 4.5: Calibration of the magnetic field: example of acquired and extracted samples

offset is independently calculated for each measure as average value of the first and last two thousand samples of the measure, since the magnetic field sensor present a continuous thermal shift that needs to be compensated. These offsets are then subtracted from the values of the currents and of the field. Furthermore, since the currents slightly differ from the theoretical value of 1 A and the field is linearly related to the current, the values of the field are normalised on the measured values of the currents. The positions, the normalised magnetic field values and their standard deviations are reported in Table 4.3

The elaborated values of the magnetic field measured in the specified positions are thus fitted to the curve representing the field along the axis of a coil, expressed by

$$B(x) = \frac{\mu_0 N r_{mean} I}{2\left(r_{mean}^2 + x^2\right)^{3/2}} \tag{4.1}$$

The values returned by the fitting procedure are reported in Table 4.4, and the results of the fitting for the two coils are depicted in Fig. 4.6.

The values obtained are slightly higher than the desired ones, but this is not a problem, since the same desired magnetic field can be generated with an even smaller current with respect to the ideal coils. It is important to notice that the two coils present slightly different values. This result is expected, since the coils are manufactured with a hand-made procedure. However, once

z(mm)	B_1(Gauss)	σ_1(Gauss)	B_2(Gauss)	σ_2(Gauss)
0	132.9799	0.1061	134.3257	0.1155
2	131.9183	0.1075	133.0588	0.0984
4	128.1285	0.1025	130.0171	0.1022
6	122.7719	0.0985	124.1930	0.0989
8	115.5508	0.1045	118.0783	0.1012
10	106.7116	0.1032	109.7480	0.0976
12	98.2116	0.1025	101.1894	0.0955
14	91.2041	0.0991	92.2754	0.0973
16	82.8935	0.0970	84.1497	0.0949
18	75.0599	0.0975	76.9722	0.0936
20	67.4445	0.0944	69.3081	0.0963
22	61.8791	0.0992	62.1484	0.0948
24	55.1820	0.0932	55.7163	0.0970
26	49.1987	0.0956	49.0091	0.0902
28	43.9678	0.0942	45.1966	0.0922
30	40.4704	0.0959	39.9386	0.0919
32	37.7320	0.0927	35.7621	0.0941
34	32.5987	0.0950	32.5411	0.0957
36	28.8995	0.0995	29.4207	0.0940
38	26.7197	0.0945	26.5885	0.0927
40	23.9660	0.0944	24.0197	0.0932

Table 4.3: Calibration of the magnetic field: experimental data

	N	r_{mean}(mm)
Coil 1	566	27.0332
Coil 2	573	26.9151

Table 4.4: Effective parameters of the coils

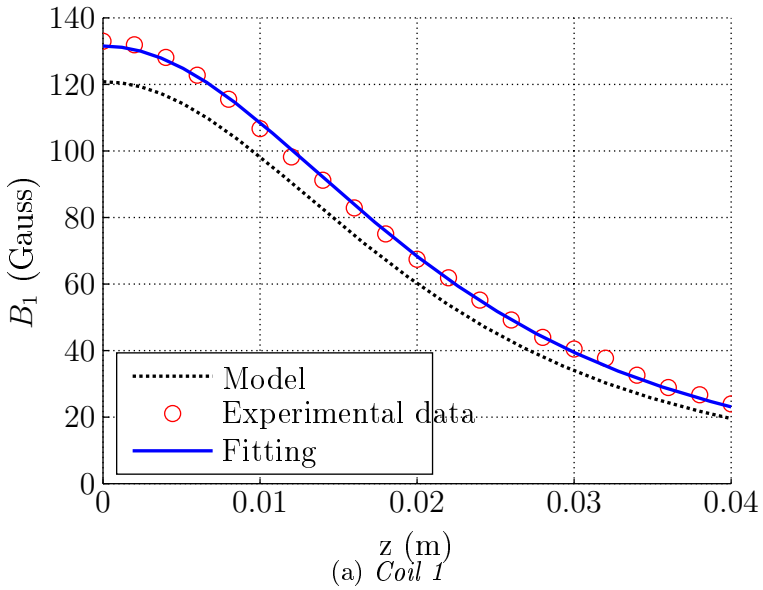

(a) *Coil 1*

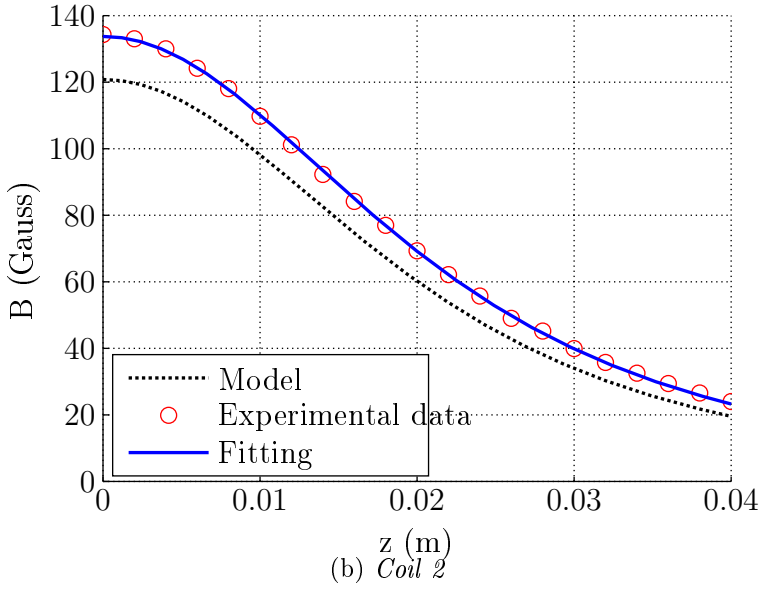

(b) *Coil 2*

Figure 4.6: Calibration of the magnetic field: fitting

these values are known, we can properly current-supply each coil in order to generate accurately controlled magnetic fields.

4.2 Validation of the systems

In the present work, three magnetic steering systems, constituted of the device for the generation of controlled magnetic fields and the three microrobot prototypes, was designed and developed. A model for each system is described in chapter 2. Here a set of tests performed on the three systems are described; moreover, a basic validation of the models is discussed.

4.2.1 The magnetic device in steering a permanent magnet

By means of the main graphical user interface described in section 3.4.2, we choose to steer the small cylindrical permanent magnet in water at various desired velocities. Considering the magnetic and geometric characteristics of the object, in fact, the interface calculates the magnetic field, and thus the currents that must flow in the coils to achieve the selected drag speed (see Appendix A). All the trials are performed by generating constant currents in the coils for ten seconds. The images of the motion are acquired at a frame rate of 10 fps.

In the first set of trials, executed selecting various speed values, the magnet did not show movement. The explanation could be one of the following two:

1. since the theoretical currents needed to achieve drag speeds of few millimetres per second are very low (about 1×10^{-6} A), the amplification stage of the magnetic device could not be able to generate the output voltage with enough precision, making the magnetic field unstable and inadequate to effectively steer the magnet;

2. the force due to the friction with the surface of the Petri dish, not considered in the model, could be comparable or even much higher than both the viscous and magnetic forces, thus blocking the movement of the magnet.

A second set of tests is performed in order to verify or avoid the first hypothesis. Two resistors are connected in series to the coils (one for each coil) to allow the amplification stage generating very low values of current with manageable values of output voltage. In these tests, as well, the magnet

have shown no movement, indicating that the absence of effective movement is not (or at least not only) due to difficulties in the generation of very low currents.

Moving from the second hypothesis, it is chosen to reduce the friction by covering the surface of the Petri dish with a film of Teflon. Then the motion tests are repeated. But the result is not changed: the magnet is still motionless.

Keeping the Teflon covering, it is tried to actuate the magnet with magnetic field gradients much higher than those predicted by the model. The object is motionless till the gradients, and thus the currents, are several (five) order of magnitude above those calculated and, then, it moves at a very high speed. This threshold behaviour can be just due to the surface friction: once overcame the surface friction force the magnet moves at the high speed due to the high applied magnetic gradient.

A final trial is performed supplying the coils with spiking currents: the pulses have negative exponential shape with a characteristic time of 20 ms, amplitude of 50000 times the theoretical currents, and a frequency of 10 Hz. By means of this excitation strategy the surface friction is overcame and the magnet moves at an observable speed. However, the data acquired with this strategy cannot be used for validating the model.

The results obtained by this set of tests suggest that the static friction force cannot be neglected for millimetre-sized objects moving in contact with a surface and that a pulsed magnetic excitation, even at low frequencies, can be used to overcome this problem.

4.2.2 The magnetic device in steering a magnetic microbead

The motion trials executed on the alginate microbeads containing superparamagnetic nanoparticles are here described. The trials are performed in water and at various desired velocities, generating constant currents in the coils and have a fixed duration of 10 s. The images of the motion are acquired at a frame rate of 10 fps.

The problems due to the surface friction found when actuating the small permanent magnet are present in the actuation of the alginate microbeads, too, since, like the magnet, they stay on the bottom of the Petri dish. Moreover, the surface of the beads is more irregular and adhesive than that of the magnet, thus increasing the importance of the problem. Also in this case, thus, the Teflon covering of the surface of the Petri dish is adopted. But, as in the case of the magnet, this solution does not grant an improvement of the

motility of the microdevice. The alginate microbeads show an instantaneous reaction to the setting of the magnetic field, which consists in an on-place rotation. This movement comes sometimes with a small instantaneous displacement due to the rotation. Then the microbeads stay motionless and keep their orientation till the end of the trial.

A possible explanation of this phenomenon is the surface friction, again. The alginate microbeads, since are fabricated by dropping, are not perfectly spherical. Moreover, the distribution of the magnetic nanoparticles is not perfectly homogeneous, as well. Hence, when dipped in a magnetic field, the bead show to have a main magnetic axis. The applied magnetic field thus leads to the observed initial alignment of the main magnetic axis of the microbead with the field, but it is not strong enough to generate a force able to overcome the friction force. Since the currents needed to move the beads even at low speeds (few millimetres per second) are quite high with respect to the maximum current that the amplifiers can supply, no trials with several order of magnitude higher currents or with high amplitude pulses can be performed. For this reason no motion data useful for the validation of the model are acquired.

Only a very qualitative test is performed on the alginate microbeads, in order to evaluate if the applied magnetic fields and gradients effectively exert a significant force on the beads. In this test an alginate magnetic microbead is put on a small (few millimetres of side) sheet of paper free-standing on the skin of the water. Then, a magnetic field like those previously employed in trying to move the microbeads in water is applied. The bead moves in the desired direction and with a velocity qualitatively comparable to the desired drag speed, demonstrating that a magnetic force is effectively applied in the right direction and with the right order of magnitude, and reinforcing the hypothesis regarding the surface friction force. The data acquired in this test cannot obviously be used for the validation of the model, since the fluid-dynamic conditions in which it is performed are not the same hypothesised in the model.

These tests underline the demand of preventing the static friction in the case of microrobots containing super-paramagnetic nanoparticles, since the forces needed to overcome the static friction force require very high magnetic fields and gradients. This can be achieved designing microrobots able to float in the fluid.

4.2.3 The magnetic device in steering a magnetic nanofilm

Finally, in the present section the motion trials executed on the polymeric nanofilms containing super-paramagnetic nanoparticles are described. As in the other tests, the trials are performed in water, at various desired velocities, generating constant currents in the coils and acquiring images at a frame rate of 10 fps. Since the maximum obtainable speeds are quite low these trials have a fixed duration of 30 s, instead of 10.

The magnetic nanofilms are nano-structured objects free-standing on the skin of water. Hence, the only force that acts on them, apart from the magnetic force, is the skin friction force, which is included in the model. As a matter of fact, no unexpected surface friction problem are encountered. In the initial stage of the trial the nanofilm rotates, demonstrating to have a main axis of magnetization due to the not perfectly homogeneous distribution of the nanoparticles, and then shifts in the desired direction and with a speed even higher than the desired one.

Six different speeds are tested and 3 trials for each desired speed value are performed, for a total of 18 trials. The images of the nanofilm motion are acquired during the trial; then the position data are extrapolated from them (see Appendix B), displayed in the interface and stored in a Matlab data file. A basic evaluation of the speed of the nanofilm and the acquired current data are displayed in the interface, too.

Subsequently, the position data acquired during the trials are analysed in order to extrapolate the speeds at the centre of the workspace and to compare them with the speeds selected through the interface.

Almost all the sets of data presents a zone around the centre of the workspace in which the trend is nearly linear (see Fig. 4.7). A linear fitting of the samples lying in this zone is performed for each set of data. Only two sets do not present a zero-crossing, probably due to problems in the position extrapolation from the images rather than to an effective problem in the movement, and they are discarded for the fitting. The procedure of fitting allows to evaluate a constant value of the speed in the zone of nearly linear trend around the centre of the workspace.

The desired speed, the value obtained by the fitting and their ratio obtainbed from the 18 trials are reported in Table 4.5.

We can observe that all the values of speed obtained by the analysis of the data are quite higher than the theoretical ones, expected by the model of motion of the nanofilm. For this object the theoretical drag speed at the

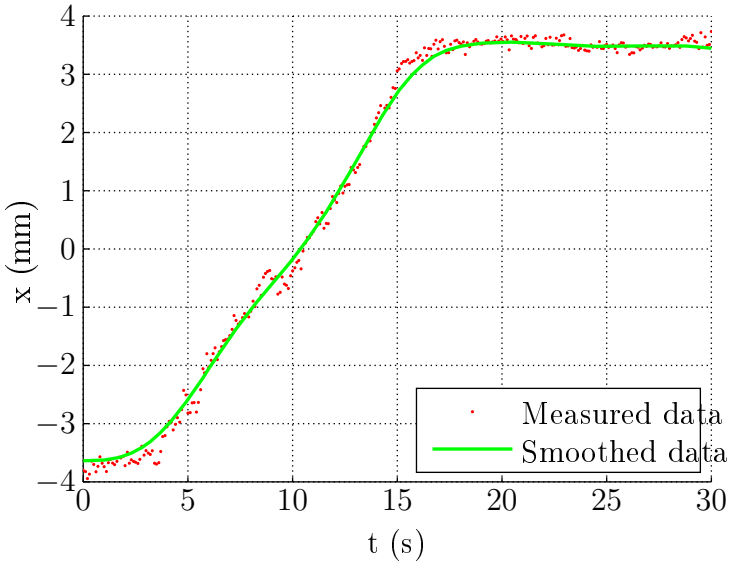

Figure 4.7: Example of position survey

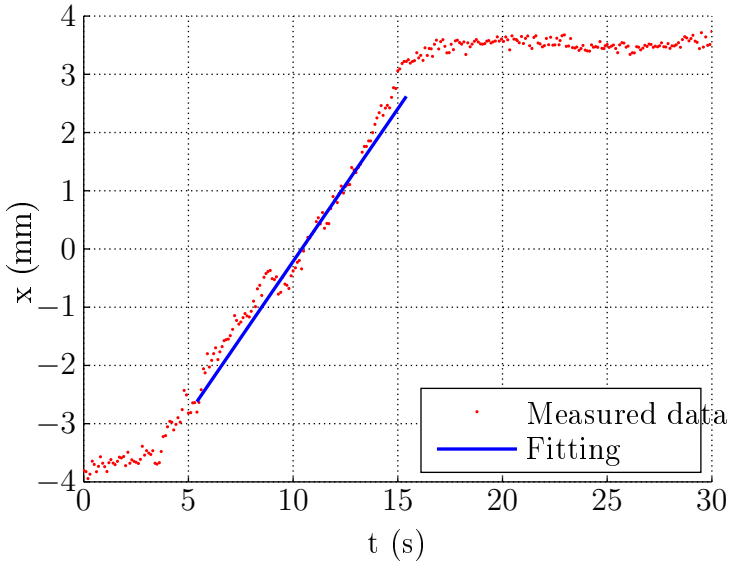

Figure 4.8: Example of speed extrapolation by fitting

$v_{theo}(\mathrm{mm}\cdot\mathrm{s}^{-1})$	$v_{fit}(\mathrm{mm}\cdot\mathrm{s}^{-1})$	*ratio*
−0.3	−0.5742	1.9140
−0.3	−0.3824	1.2746
−0.3	−0.3807	1.2689
−0.2	−0.3869	1.9346
−0.2	−0.4099	2.0497
−0.2	−0.3692	1.8461
−0.1	−0.1676	1.6757
−0.1	–	–
−0.1	–	–
+0.1	+0.1865	1.8648
+0.1	+0.2506	2.5061
+0.1	+0.1687	1.6866
+0.2	+0.4644	2.3220
+0.2	+0.4099	2.0495
+0.2	+0.2087	1.0437
+0.3	+0.4831	1.6103
+0.3	+0.5101	1.7004
+0.3	+0.6009	2.0029

Table 4.5: Evaluated speeds for a nanofilm

centre of the workspace is expressed by equation 2.68, namely

$$v_0\left(I_f, I_g\right) \cong \left[\frac{768\sqrt{3}}{2401}\frac{\chi_p d_p h l^{1/2}}{\zeta\left(\rho_f \mu_f\right)^{1/2}}\frac{\mu_0^2 N^2}{R^3} I_f I_g\right]^{2/3}$$

Finally, the speeds obtained by the fitting procedures are normalised on the theoretical speeds in order to obtain a proportionality coefficient. The mean value of this ratio among the trials is

$$\frac{v_{fit}}{v_{theo}} = 1.7969 \pm 0.38109$$

This result is probably due to uncertainties in the fabrication process of nanofilms. These are, mainly:

- density of nanoparticles differing from the theoretical one, because of the sedimentation of the super-paramagnetic nanoparticles in suspension;

- not uniform distribution of the super-paramagnetic nanoparticles and, thus, formation of a main axis of magnetization; this can be observed in the performed trials, in which the nanofilm orients itself always in the same direction.

Conclusions and future developments

In the present work the study and development of three hypothetical magnetic steering systems is performed by designing a device for the generation of controlled magnetic fields and employing it in the actuation of three microrobot prototypes.

The magnetic field generating device is designed and dimensioned in order to employ it as a component of a magnetic steering system for microrobots. The developed device is validated and it has shown the following abilities:

- generation of static magnetic fields and gradients controlled by the user;
- calculation of the requested magnetic fields in order to obtain a desired motion speed, on the basis of a model of interaction between the generated magnetic fields and the object;
- real-time visualization and acquisition of the images of the workspace;
- off-line individuation of the object position by means of image elaboration;
- evaluation of the performances of magnetic steering systems;
- storing of experimental data.

The magnetic field generator is a platform used for testing the propulsion of various microrobot prototypes by the pulling propulsion method. Moreover, by means of the abilities of real-time images acquisition and elaboration, the platform has allowed an evaluation of the performances of the tested systems. The developed test platform is, thus, a tool that could be employed in the design and preliminary performance evaluation of future magnetic steering systems.

Three different models of interaction between the generated magnetic field and three microrobot prototypes, which are a permanent magnet, a

polymeric microbead and a nanofilm, both loaded with super-paramagnetic nanoparticles, are developed. The model of motion of the nanofilm is validated, since it predicts direction and speed of motion of nanofilms. No useful results are obtained for the models of motion of the permanent magnet and of the microbeads containing super-paramagnetic particles, because of static friction. However, all the tests have highlighted some critical aspects that must be considered in the design and development of future magnetic steering systems for microrobots.

Future developments will regard the performances and capabilities of the test platform; in particular the microrobot localization stage could be improved both enhancing the image elaboration process and, in the case of nanofilms, employing coloured nanofilms. The image elaboration process could also be optimised, in order to allow real-time localization and tracking of the actuated microdevice. Furthermore, in order to design clinically applicable magnetic steering systems, a control loop based on a position feedback, which requires real-time tracking, needs to be implemented. Furthermore, in the case of cardiovascular applications, an innovative non-optic localization method needs to be developed.

Finally, the future medical magnetic microrobots should be floating, preventing static friction. In particular permanent magnets are too heavy to float in body fluids. Their employment in swimming medical microrobots is thus not suitable. Their embedding in polymeric structures could be considered, in order to avoid friction and sticking effects. The smallest commercial permanent magnets have typical sizes of millimetres, which are not adapt for microrobotics. The embedding of super-paramagnetic nanoparticles in polymeric object demonstrated to be a feasible way for fabricating microdevices steerable by magnetic fields. Thus, magnetic-swimming microrobots able to float in body fluids can be obtained embedding super-paramagnetic particles in floating polymeric structures with a wide size range. Moreover, since each particle is subjected to a different magnetic force, which depends on the local magnetic field and gradient, if embedded in a highly deformable structure, the resulting microrobot could be able to change its shape. Such kind of deformation, obtainable also with static magnetic fields and gradients, could facilitate the propulsion of microrobots in body fluids, both decreasing the viscous forces and allowing the transit through small openings or blood vessels.

Appendix A

Calculation of the currents

The main software interface, presented in section 3.4.2, allows the control of the microrobot prototypes for the motion trials; selecting the type of microrobot prototype and specifying its sizes and the desired drag speed at the centre of the workspace, the program automatically calculates and visualizes the currents that must flow in the coils in order to generate the needed magnetic field and thus the requested velocity. The ideal and expected values of drag speed, magnetic induction field and gradient are calculated along the workspace and visualized in three different graphs. These calculations are performed before the effective execution of the trial by calling an external Matlab script and they enable the execution of the specified trial.

This step is of fundamental importance, since different microrobot prototypes with different sizes obviously needs different fields and gradients, and thus different currents, to move at a same speed. Furthermore, the drag speed at the centre of the workspace can be chosen for each trial by the user. Finally, in this stage the non-idealness of the coils are considered and compensated.

A.1 Calculation of the ideal field and gradient

First of all, once selected the object and its size, and knowing the relative magnetic parameters, the program calculates the magnetic induction field and field gradient at the centre of the workspace needed to obtain the desired drag speed. These are called "ideal" field and gradient, since the "real" field and gradient, as described below, will coincide with the ideal one only in the centre of the workspace. The same is for the drag speed.

The ideal field and gradient are calculated considering the three models of motion of the microrobot prototypes described in chapter 2. For this reason,

three different Matlab scripts, one for each kind of microrobot prototype, are developed and selectively recalled.

A.1.1 Permanent magnet

The terminal speed of a permanent magnet steered by static magnetic fields and gradients is directly proportional to the applied magnetic field gradient, as described by equation 2.54

$$v_0 \left(\nabla B_0\right) = \frac{rh}{6\mu_f} M \cdot \nabla B_0$$

from which the value of the ideal gradient can be easily obtained, as expressed by

$$\nabla B_0^{id} = \frac{6_f}{rhM} v_0^{id} \tag{A.1}$$

It is important to notice that there is not any dependence from the value of the ideal magnetic field.

A.1.2 Alginate sphere

For a polymeric bead containing super-paramagnetic nanoparticles the situation is different: in this case the drag speed is function of both the applied magnetic field and gradient, as expressed by equation 2.61

$$v_0 \left(B_0, \nabla B_0\right) = \frac{4}{9} \frac{\chi_p d_p r^2}{\mu_f} B_0 \nabla B_0$$

Hence, we have only one condition and two variables to solve. For this reason we need to impose an arbitrary second condition in order to univocally determine both the field and the gradient. The choice made in this work is to generate an ideal uniform magnetic field that allows having a positive field along all the workspace, even in presence of a field gradient. Thus, the magnetic field can be expressed in function of the magnetic gradient as

$$B_0^{id} = \frac{L_{WS}}{2} \left|\nabla B_0^{id}\right| \tag{A.2}$$

Consequently equation 2.61 can be rewritten as

$$\left|v_0^{id} \left(\nabla B_0^{id}\right)\right| = \frac{4}{9} \frac{\chi_p d_p r^2}{\mu_f} \frac{L_{WS}}{2} \left(\nabla B_0^{id}\right)^2 \tag{A.3}$$

which in turn gives

$$\left|\nabla B_0^{id}\right| = \frac{3}{r}\sqrt{\frac{\mu_f}{2\chi_p d_p L_{WS}}\left|v_0^{id}\right|} \tag{A.4}$$

The respective magnetic field can thus be obtained as

$$B_0^{id} = \frac{3}{2r}\sqrt{\frac{\mu_f L_{WS}}{2\chi_p d_p}\left|v_0^{id}\right|} \tag{A.5}$$

It is important to notice that the value of the magnetic field is always positive, while the gradient has the same sign as the desired drag speed.

A.1.3 Nanofilm

The case of a nanofilm containing super-paramagnetic nanoparticles is analogous to that polymeric bead one, since the magnetic interaction is mediated by the same iron oxide particles. Moving from equation 2.68

$$\left|v_0\left(B_0, \nabla B_0\right)\right| = \left[\frac{2\chi_p d_p h l^{1/2}}{\zeta\left(\rho_f \mu_f\right)^{1/2}} B_0 \left|\nabla B_0\right|\right]^{2/3}$$

where the speed and the gradient have the same sign and the field is always positive, considering the same assumption as above

$$B_0^{id} = \frac{L_{WS}}{2}\left|\nabla B_0^{id}\right|$$

we obtain

$$\left|v_0^{id}\left(\nabla B_0^{id}\right)\right| = \left[\frac{2\chi_p d_p h l^{1/2}}{\zeta\left(\rho_f \mu_f\right)^{1/2}} \frac{L_{WS}}{2}\left(\nabla B_0^{id}\right)^2\right]^{2/3} \tag{A.6}$$

from which the needed magnetic field gradient can be calculated, as expressed by

$$\left|\nabla B_0^{id}\right| = \sqrt{\frac{\zeta\left(\rho_f \mu_f\right)^{1/2}}{\chi_p d_p h l^{1/2} L_{WS}}\left|v_0^{id}\right|^{3/2}} \tag{A.7}$$

A.2 Calculation of the currents

The currents that have to flow in the coils in order to generate the obtained values of the magnetic field and gradient at the centre of the workspace can be now calculated.

Moving from the effective parameters of the coils, the magnetic field and gradient along the workspace of the effective system can be expressed as

(A.8)

$$B\left(x,i_1,i_2\right)=\frac{\mu_0}{2}\left\{\frac{N_1 r_{mean,1}^2}{\left[r_{mean,1}^2+\left(x+\frac{L}{2}\right)^2\right]^{3/2}}i_1+\frac{N_2 r_{mean,2}^2}{\left[r_{mean,1}^2+\left(x-\frac{L}{2}\right)^2\right]^{3/2}}i_2\right\}$$

(A.9)

$$\frac{dB}{dx}\left(x,i_1,i_2\right)=-\frac{3\mu_0}{2}\left\{\frac{N_1 r_{mean,1}^2\left(x+\frac{L}{2}\right)}{\left[r_{mean,1}^2+\left(x+\frac{L}{2}\right)^2\right]^{5/2}}i_1+\frac{N_2 r_{mean,2}^2\left(x-\frac{L}{2}\right)}{\left[r_{mean,2}^2+\left(x-\frac{L}{2}\right)^2\right]^{5/2}}i_2\right\}$$

we can obtain the real values of the magnetic field and gradient at the centre of the workspace, as expressed by

(A.10) $$B_0\left(i_1,i_2\right)=4\mu_0\left[\frac{N_1 r_{mean,1}^2}{\left(4r_{mean,1}^2+L^2\right)^{3/2}}i_1+\frac{N_2 r_{mean,2}^2}{\left(4r_{mean,2}^2+L^2\right)^{3/2}}i_2\right]$$

(A.11)

$$\nabla B_0\left(i_1,i_2\right)=24\mu_0 L\left[-\frac{N_1 r_{mean,1}^2}{\left(4r_{mean,1}^2+L^2\right)^{5/2}}i_1+\frac{N_2 r_{mean,2}^2}{\left(4r_{mean,2}^2+L^2\right)^{5/2}}i_2\right]$$

These equations can be rearranged to obtain two apparently independent conditions

(A.12) $$B_0\left(I_f\right)=8\mu_0\frac{N_1+N_2}{r_{mean,1}+r_{mean,2}}I_f$$

(A.13) $$\nabla B_0\left(I_g\right)=192\mu_0 L\frac{N_1+N_2}{\left(r_{mean,1}+r_{mean,2}\right)^3}I_g$$

in which we impose

(A.14)
$$I_f = \frac{1}{2}\frac{r_{mean,1}+r_{mean,2}}{N_1+N_2}\left[\frac{N_1 r_{mean,1}^2}{\left(4r_{mean,1}^2+L^2\right)^{3/2}}i_1+\frac{N_2 r_{mean,2}^2}{\left(4r_{mean,2}^2+L^2\right)^{3/2}}i_2\right]$$

(A.15)
$$I_g = \frac{1}{8}\frac{\left(r_{mean,1}+r_{mean,2}\right)^3}{N_1+N_2}\left[-\frac{N_1 r_{mean,1}^2}{\left(4r_{mean,1}^2+L^2\right)^{5/2}}i_1+\frac{N_2 r_{mean,2}^2}{\left(4r_{mean,2}^2+L^2\right)^{5/2}}i_2\right]$$

Once obtained the currents I_f and I_g from equations A.12, the currents i_1 and i_2 flowing, respectively in the left and in the right coil can thus be calculated.

A.3 Calculation of the real speed, field and gradient

The obtained values for the currents flowing in the coils are then used to current-supply the device for the generation of controlled magnetic fields. Moreover, the real speed, field and gradient along the workspace are calculated, moving from the obtained currents, and returned to the interface, as well.

The expected magnetic field and gradient along the workspace are calculated substituting the currents in equations A.8. These results are then employed to calculate the expected drag speed along the workspace from equations 2.54, 2.61 and 2.68, respectively for the case of the permanent magnet, of the alginate sphere and of the nanofilm.

Appendix B

Image data elaboration

B.1 Thresholding of the images

Here the procedure for the elaboration of the images of motion trials on three microrobot prototypes is described. The images are acquired and stored during the trial and subsequently elaborated by an algorithm developed in Matlab, in order to extract the information regarding the position of the tested magnetic microdevice. This elaboration is performed just after the effective trial and the results are immediately displayed in the second page of the window interface.

First of all, each image (1600×300 pixels obtained with a 4× hardware vertical binning and thus corresponding to 1600×1200 pixels) is imported and a preliminary noise cleaning is performed. Both a median (3×3 neighborhood) and an average (5×5 convolution kernel) filter are used, thus obtaining a reduction of both the shot and the Gaussian random noises. These operations are performed in order to prevent the arising of artefacts during the subsequent steps of elaboration. The smoothing of the images caused by the application of the average filter is not a problem for the purpose of the elaboration.

Although the employment during the trials of a dedicated illumination of the workspace, the acquired images present a non-homogeneous background, which can be problematic in the thresholding stage. In order to prevent errors due to the non homogeneity of the background, its local value is calculated and subtracted from the image by means of a custom developed function. This operation dramatically increases the accuracy of the object individuation process; however, if the images are not acquired with a proper lighting, the results of the background subtraction and of the whole object individuation process are not satisfactory. Furthermore, this is a critical elaboration

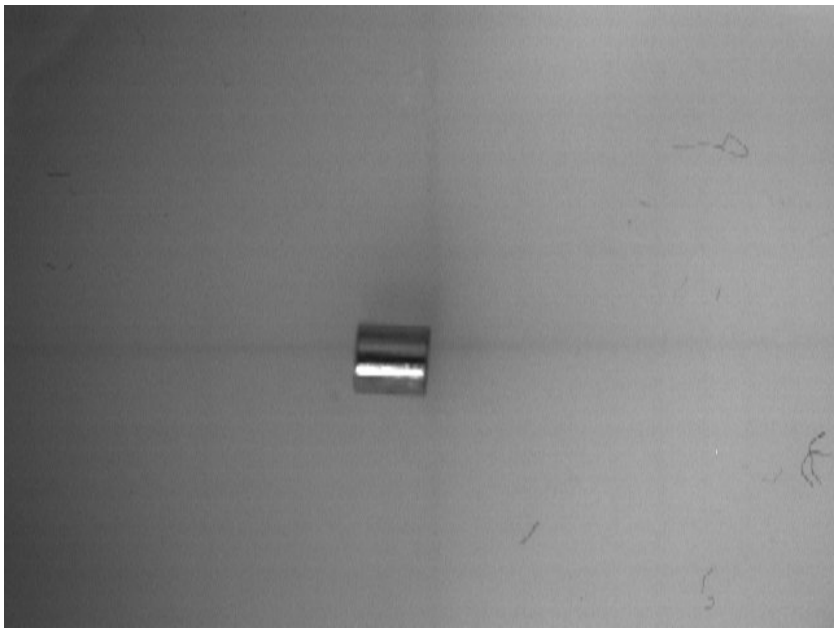

(a) *original*

(b) *filtered*

Figure B.1: Original and filtered image

step for individuating nearly-transparent objects like the employed magnetic nanofilms.

Figure B.2: Image after background subtracting

The images resulting from the background subtraction are then subjected again to a noise cleaning with both a median (3×3 neighborhood) and an average (15×15 convolution kernel) filter, in order to eliminate eventual local errors due to the previous operation. Finally, the effective thresholding of the images is performed, obtaining black and white binary images. The threshold is automatically calculated by a Matlab Image Processing Toolbox function.

B.2 Individuating the objects

The result of the thresholding operation is a black and white binary image. Since all the objects are darker than the background, in the thresholded images the object is black, while the background is white. The position of the centre of mass of the object is thus considered to be in the centre of the black area.

The objects have different shapes and, moreover, in the case of nanofilms, which are nearly transparent, the previous described elaboration strategy do not produce a single uniform black area, but rather a series of small black spots coinciding with single or aggregated iron oxide nanoparticles dispersed

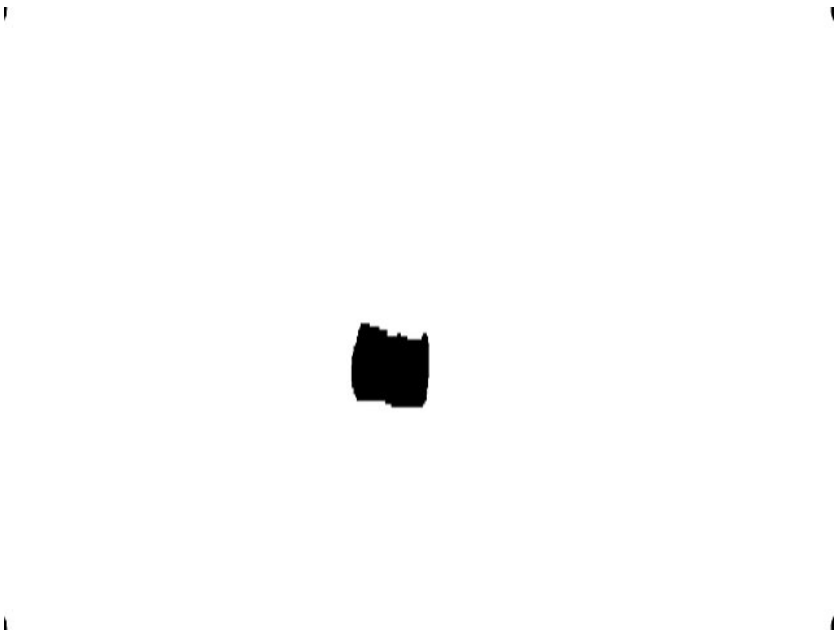

Figure B.3: Thresholded image

in the film. For this reason the simple employment of built-in procedures for the recognition of specific shapes is avoided. Instead, the used procedure is the following: all the black zones are segmented and the relative geometrical centres are individuated, then these points are used to calculate the expected centre of mass. This point is assumed to coincide with the real centre of mass of the object. However, this relatively easy method for centre of mass individuation presents some limitations that can lead, in some case, to not accurate results; In fact the calculation of the point of interest is based on the assumption that the centre of mass exactly coincides with the geometrical centre of the black zones. This assumption is not verified in the following cases:

- errors in the thresholding process due to high variability of the brightness of the background;
- presence of light reflections in the image that alter the individuated shape of the object;
- not uniform distribution of the nanoparticles (in the case of nanofilms).

The results of the individuation process performed on all the set of images relative to a single trial are then stored in a vector containing the evaluated positions of the object during the entire trial. These values directly obtained

by the individuation process are considered raw data and are displayed in the interface as a dispersion of points. The time derivative of the position is then numerically calculated to obtain the raw speed data, displayed in another graph as a dispersion of point. Starting from these raw data, smoothed position and speed trends are also calculated and then displayed in the interface. Smoothed data are represented with solid lines in the respective graphs, superimposed on the respective raw data.

Due to the limitation of the presented algorithm particular attention in using it have been paid and a manual control of the less coherent trial results have been done.

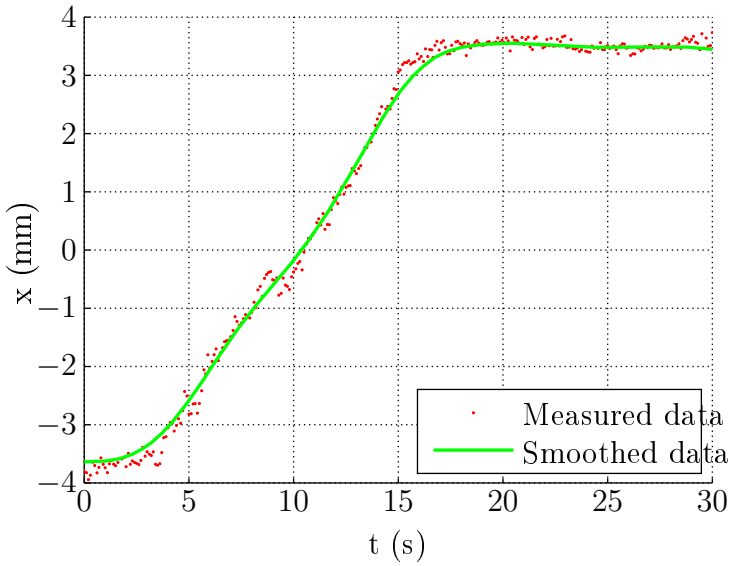

Figure B.4: Raw and smoothed data

Bibliography

[1] J.J. Abbott, Z. Nagy, F. Beyeler, and B.J. Nelson. Robotics in the small. *IEEE Robotics & Automation Magazine*, 14(2):92–103, June 2007. http://dx.doi.org/10.1109/MRA.2007.380641.

[2] J.J. Abbott, K.E. Peyer, L. Dong, and B.J. Nelson. How should microrobots swim? In *13th International Symposium of Robotics Research, Hiroshima, Japan*, 2007.

[3] J.J. Abbott, K.E. Peyer, M.C. Lagomarsino, L. Zhang, L. Dong, I.K. Kaliakatsos, and B.J. Nelson. How should microrobots swim? *International Journal of Robotics Research*, 28(11-12):1434–1447, 2009. http://dx.doi.org/10.1177/0278364909341658.

[4] D.J. Bell, S. Leutenegger, K.M. Hammar, L.X. Dong, and B.J. Nelson. Flagella-like propulsion for microrobots using a nanocoil and a rotating electromagnetic field. In *Robotics and Automation, 2007 IEEE International Conference on*, pages 1128–1133, 2007. http://dx.doi.org/10.1109/ROBOT.2007.36313.

[5] R.P. Blakemore. Magnetotactic bacteria. *Annual Review of Microbiology*, 36:217–238, 1982. http://dx.doi.org/10.1146/annurev.mi.36.100182.001245.

[6] F. Carpi and C. Pappone. Stereotaxis niobe®magnetic navigation system for endocardial catheter ablation and gastrointestinal capsule endoscopy. *Expert Review of Medical Devices*, 6(5):487–498, September 2009. http://dx.doi.org/10.1586/erd.09.32.

[7] H. Choi, J. Choi, G. Jang, J.-0. Park, and S. Park. Two-dimensional actuation of a microrobot with a stationary two-pair coil system. *Smart Materials and Structures*, 18, March 2009. http://dx.doi.org/10.1088/0964-1726/18/5/055007.

[8] H. Choi, C. Yu, H. Bae, J.-0. Park, and S. Park. Theoretical analysis and experimental validation dor electromagnetic based actuation of microrobot. In *39th International Symposium on Robotics 2008*, pages 96–99, 2008.

[9] P. Dario, R. Valleggi, M.C. Carrozza, M.C. Montesi, and M. Cocco. Microactuators for microrobots: a critical survey. *Journal of Micromechanics and Microengineering*, 2:141–157, 1992. `http://dx.doi.org/10.1088/0960-1317/2/3/005`.

[10] R. Dreyfus, J. Baudry, M.L. Roper, M. Fermigier, H.A. Stone, and J. Bibette. Microscopic artificial swimmers. *Nature*, 437(7060):862–865, 2005. `http://dx.doi.org/10.1038/nature04090`.

[11] E.H. Frei. Magnetism and medicine. *Journal of Applied Physics*, 40(3), March 1969. `http://dx.doi.org/10.1063/1.1657801`.

[12] E.H. Frei, S. Leibinzohn, and H.N. Neufeld. The 'pod', a new magnetic device for medical application. In *Proc. 16th Conf. Eng. Med. Biol*, 1963.

[13] T. Fujie, Y. Okamura, and S. Takeoka. Ubiquitous transference of a free-standing polysaccharide nanosheet with the development of a nano-adhesive plaster. *Advanced Materials*, 19(21):3549–3553, 2007. `http://dx.doi.org/10.1002/adma.200700661`.

[14] Y. Ganji, F. Janabi-Sharifi, and A.N. Cheema. Robot-assisted catheter manipulation for intracardiac navigation. *International Journal of Computer Assisted Radiology and Surgery*, 4(4):307–315, June 2009. `http://dx.doi.org/10.1007/s11548-009-0296-z`.

[15] S. Guo, Q. Pan, and M.B. Khamesee. Development of a novel type of microrobot for biomedical application. *Microsystem Technologies*, 14(3):307–314, March 2008. `http://dx.doi.org/10.1007/s00542-007-0430-1`.

[16] D. Halliday and R. Resnick. *Fundamental of Physics*. Wiley & Sons Ltd., 2007.

[17] T. Honda, K.I. Arai, and K. Ishiyama. Micro swimming mechanisms propelled by external magnetic fields. *Magnetics, IEEE Transactions on*, 32(5):5085–5087, September 1996. `http://dx.doi.org/10.1109/20.539498`.

[18] K. Ishiyama, K.I. Arai, M. Sendoh, and A. Yamazaki. Spiral-type micro-machine for medical applications. *Journal of Micromechatronics*, 2(1):77–86, 2002. http://dx.doi.org/10.1163/156856302766647161.

[19] M.B. Khamesee, N. Kato, Y. Nomura, and T. Nakamura. Design and control of a microrobotic system using magnetic levitation. *IEEE/ASME Transaction on Mechatronics*, 7(1):1–14, March 2002.

[20] S. Martel, J.-B. Mathieu, O. Felfoul, H. Macicior, G. Beaudoin, G. Soulez, and L.H. Yahia. Adapting mri systems to propel and guide microdevices in the human blood circulatory system. In *Engineering in Medicine and Biology Society, 2004. IEMBS '04. 26th Annual International Conference of the IEEE*, volume 1, pages 1044–1047, 2004. http://dx.doi.org/10.1109/IEMBS.2004.1403342.

[21] J.-B. Mathieu, G. Beaudoin, and S. Martel. Method of propulsion of a ferromagnetic core in the cardiovascular system through magnetic gradients generated by an mri system. *IEEE Transactions on Biomedical Engineering*, 53(2):292–299, February 2006. http://dx.doi.org/10.1109/TBME.2005.862570.

[22] J.-B. Mathieu, S. Martel, L. Yahia, G. Soulez, and G. Beaudoin. Preliminary studies for using magnetic resonance imaging systems as a mean of propulsion for microrobots in blood vessels and evaluation of ferromagnetic artefacts. In *Electrical and Computer Engineering, 2003. IEEE CCECE 2003. Canadian Conference on*, volume 2, pages 835–838, 2003. http://dx.doi.org/10.1109/CCECE.2003.1226024.

[23] V. Mattoli, V. Pensabene, T. Fujie, S. Taccola, A. Menciassi, S. Takeoka, and P. Dario. Fabrication and characterization of ultra-thin magnetic films for biomedical applications. In *Eurosensors XXIII, Lausanne*, pages 28–31, 2009.

[24] V. Mattoli, E. Sinibaldi, V. Pensabene, S. Taccola, A. Menciassi, and P. Dario. Magnetic nanosheets manipulation: modeling, development and validation. In *Robotics and Automation, 2010. ICRA 2010. IEEE International Conference on.* submitted.

[25] B.J. Nelson. Microrobotics in medicine. In *JournÃl'es Nationales de la Recherche en Robotique*, 2007. http://dx.doi.org/10.1.1.98.994-2.

[26] Y. Okamura, S. Utsunomiya, H. Suzuki, D. Niwa, T. Osaka, and S. Takeoka. Fabrication of free-standing nanoparticle-fused nanosheets

and their hetero-modification using sacrificial film. *Colloids and Surfaces A: Physicochemical and Engineering Aspects*, 318(1-3):184–190, April 2008. http://dx.doi.org/10.1016/j.colsurfa.2007.12.049.

[27] S. Park and J.-O. Park. Frontier research program on biomedical microrobot for intravascular therapy. In *Biomedical Robotics and Biomechatronics, 2008. BioRob 2008. 2nd IEEE RAS & EMBS International Conference on*, pages 360–365, 2008. http://dx.doi.org/10.1109/BIOROB.2008.4762933.

[28] E.M. Purcell. Life at low reynolds number. *American Journal of Physics*, 45(1):3–11, January 1977. http://dx.doi.org/10.1119/1.10903.

[29] L. Rubinstein. A practical nanorobot for treatment of various medical problems. In *Eighth Foresight Conference on Molecular Nanotechnology*, 2000.

[30] S. Rudin, D.R. Bednarek, and K.R. Hoffmann. Endovascular image-guided interventions (eigis). *Medical Physics*, 35(1):301–309, January 2008. http://dx.doi.org/10.1118/1.2821702.

[31] B. Schmidt, K.R. Chun, R.R. Tilz, B. Koektuerk, F. Ouyang, and K.H. Kuck. Remote navigation systems in electrophysiology. *Europace*, 10(3):iii57–iii61, November 2008. http://dx.doi.org/10.1093/europace/eun234.

[32] M. Sendoh, N. Ajiro, K. Ishiyama, M. Inoue, and K.I. Arai. Effect of machine shape on swimming properties of the spiral-type magnetic micromachine. *IEEE Transactions on Magnetics*, 35(5):3688–3690, September 1999.

[33] M. Sitti. Microscale and nanoscale robotics systems [grand challenges of robotics]. *Robotics & Automation Magazine, IEEE*, 14(1):53–60, March 2007. http://dx.doi.org/10.1109/MRA.2007.339606.

[34] S. Sudo, S. Segawa, and T. Honda. Magnetic swimming mechanism in a viscous liquid. *Journal of Intelligent Material Systems and Structures*, 17(8-9):729–736, September 2006. http://dx.doi.org/10.1177/1045389X06055828.

[35] H. Tillander. Magnetic guidance of a catheter with articulated steel tip. *Acta Radiology*, 35(1):62–64, January 1951.

[36] F.M. White. *Viscous fluid flow*. McGraw-Hill, 2005.

[37] K.B. Yesin, K. Vollmers, and B.J. Nelson. Modeling and control of untethered biomicrorobots in a fluidic environment using electromagnetic fields. *International Journal of Robotics Research*, 25(5-6):527–536, 2006. http://dx.doi.org/10.1177/0278364906065389.

[38] L. Zhang, J.J. Abbott, L. Dong, B.E. Kratochvil, D. Bell, and B.J. Nelson. Artificial bacterial flagella: Fabrication and magnetic control. *Applied Physics Letters*, 94(6), February 2009. http://dx.doi.org/10.1063/1.3079655.